arXiv:1411.0916v1 [hep-ph] 4 Nov 2014

Electroweak corrections to lepton pair production in association with two hard jets at the LHC

A. Denner[1], L. Hofer[2], A. Scharf[1], S. Uccirati[3]

[1] *Universität Würzburg, Institut für Theoretische Physik und Astrophysik, D-97074 Würzburg, Germany*

[2] *Institut de Física d'Altes Energies (IFAE) Edifici Cn, Universitat Autònoma de Barcelona (UAB), E-08193 Bellaterra (Barcelona), Spain*

[3] *Università di Torino, Dipartimento di Fisica, Italy INFN, Sezione di Torino, Italy*

Abstract:

We compute the next-to-leading order corrections of $\mathcal{O}(\alpha_s^2\alpha^3)$ to the hadronic production of two oppositely charged leptons and two hard jets, $pp \to jj\ell^-\ell^+$, using Recola and Collier. We include electroweak and QCD corrections at the given order and all off-shell effects. We provide detailed predictions for the LHC operating at 13 TeV and obtain per-cent-level corrections for the total cross section. For differential distributions we find significant non-uniform distortions in high-energy tails at the level of several ten per cent due to electroweak Sudakov logarithms and deformations at the level of a few per cent for angular variables.

November 2014

1 Introduction

After the discovery of the Higgs boson, the search for physics beyond the Standard Model (SM) is the primary goal of the Large Hadron Collider (LHC). The lack of evident phenomena of new physics at the TeV scale calls for a precise study of the SM in order to reveal possible small deviations between theory and experiment. This can be achieved through sophisticated experimental analyses, capable of highlighting a small signal on a huge background, whose knowledge is essential to interpret the data. Sometimes data are not sufficient for an accurate estimation of the background and theoretical descriptions become important. Moreover, data-driven determinations of the background often rely on extrapolations to the signal region based on theoretical distributions. Minimising theoretical uncertainties becomes therefore necessary not only for the signal processes, but also for all those processes that can contribute to the background.

In order to achieve the needed precision, leading-order (LO) predictions in perturbation theory are not sufficient for most cases. At hadron colliders QCD corrections can be of the order of several ten per cent and have been carefully studied for many processes. Electroweak (EW) corrections are often small for inclusive observables; nevertheless they can have an important impact and should thus be studied carefully. In particular, they are typically strongly enhanced in high-energy tails of distributions, where for the first time the LHC will collect enough data to see the effects of sizable logarithms of EW origin. Moreover, in particular cases like Higgs production in vector-boson fusion, EW corrections can be of the same order of magnitude as QCD corrections [1]. For these reasons EW corrections represent the next frontier of next-to-leading-order (NLO) calculations for LHC physics, as pointed out by the most recent Les Houches Wish-list [2].

In the past years, many groups have concentrated their efforts to make NLO calculations feasible, and a lot of codes have been designed [3–11] with a high level of automatisation and impressive performances, however with their range of applicability mostly restricted to the QCD sector of the SM. For EW corrections, the situation is more involved and a complete automatisation has not been achieved yet, while different groups are working in this direction [12, 13]. Recently we have developed the code Recola [14,15] which performs efficient calculations of tree-level and one-loop amplitudes in the full SM. Recola uses an alternative approach to Feynman diagrams, based on recursion relations for off-shell currents. The algorithm, originally proposed by Andreas van Hameren in Ref. [16] for gluonic amplitudes, is based on the decomposition of one-loop amplitudes as linear combinations of tensor integrals, whose coefficients are calculated recursively. The tensor integrals are computed by linking Recola to the Collier library [17,18], which provides one-loop scalar and tensor integrals for arbitrary scattering processes.

A class of SM background processes, particularly important for searches of new physics, is the production of a weak boson accompanied by jets ($pp \to W/Z + \text{jets}$). If for example the Z boson decays into neutrinos, the process $Z + 2\,\text{jets}$ has the same signature (missing energy plus 2 jets) as the production of a pair of squark and anti-squark, each subsequently decaying into a jet and an invisible neutralino. Such events are mainly searched for in high-energy regions, where EW corrections are usually sizable. The experimental estimation of the irreducible SM background is obtained by data-driven extrapolations from measured control samples, where the gauge boson decays into charged leptons. The process $pp \to Z + 2\,\text{jets} \to \ell^-\ell^+ + 2\,\text{jets}$ is a typical ingredient in these studies. Moreover, the production of a Z boson with two jets provides an important background to Higgs-boson production in vector-boson fusion [19, 20]. The signature of the Higgs signal consists typically of two jets in forward and backward rapidity regions and a Higgs boson decaying in the central region of the detector. Analysing the process $pp \to Z + 2\,\text{jets}$ $\to \ell^-\ell^+ + 2$ jets in this kinematic region offers the possibility to carefully study the systematics

of the H + 2 jets final state. Analyses of LHC data with an integrated luminosity of $5\,\text{fb}^{-1}$ at 7 TeV and $20\,\text{fb}^{-1}$ at 8 TeV have appeared in Refs. [21–23] for Z production in association with jets. Moreover, the pure EW contribution to Z production with two jets has been measured by the ATLAS and CMS collaboration at 7 TeV and 8 TeV [24–26].

The LO amplitude of the process $\text{pp} \to \ell^-\ell^+ + 2\,\text{jets}$ gets contributions from pure EW tree-level diagrams on top of the dominant diagrams involving gluons (QCD tree level). The QCD corrections to the LO QCD contributions have been investigated in Refs. [27, 28], while QCD corrections to EW LO contributions with vector-boson-fusion topology have been computed in Ref. [20]. The QCD corrections to the total cross section turn out to be of the order of 10%. The NLO QCD calculations have been matched to parton showers both for the QCD mediated processes [29, 30] and the vector-boson-fusion-mediated processes [31, 32]. In Ref. [14] we performed a first study of EW corrections to the process $\text{pp} \to \text{Z} + 2\,\text{jets}$ with an on-shell Z boson. Restricting our attention to the dominant partonic processes involving external gluons, $q\,\text{g} \to q\,\text{g}\,\text{Z}$, $\bar{q}\,\text{g} \to \bar{q}\,\text{g}\,\text{Z}$, $\text{g}\,\text{g} \to q\,\bar{q}\,\text{Z}$, $q\,\bar{q} \to \text{g}\,\text{g}\,\text{Z}$, we found small EW effects on the total cross section at the level of -1%, while transverse-momentum distributions received enhanced corrections at high p_T (up to -25% for $p_\text{T} \simeq 1\,\text{TeV}$), owing to EW Sudakov logarithms. The large effects of EW logarithms have been also studied in next-to-leading logarithmic approximation for $\text{pp} \to \text{jj}\nu\bar{\nu}$ in Ref. [33]. For the production of a vector boson with one jet the complete EW corrections are available [34–36].

In this paper we perform a complete study of EW corrections of $\mathcal{O}(\alpha_s^2\alpha^3)$ for the process $\text{pp} \to \ell^-\ell^+ + 2\,\text{jets}$. In Section 2 the framework of our calculation is presented (Section 2.1,Section 2.2), as well as the results of the leading-order computation (Sections 2.3, 2.4). The EW NLO corrections are analysed in Section 3: the calculation of the virtual and real corrections is sketched in Sections 3.2 and 3.3 respectively; in Sections 3.4 and 3.5 the results at NLO are presented for standard acceptance cuts and vector-boson-fusion cuts. Finally, Section 4 contains our conclusions, and in App. A our implementation of photon fragmentation is described.

2 Production of $\text{pp} \to \text{jj}\ell^-\ell^+$ in LO at the LHC

In this section we define the general setup of our computation and describe basic features of lepton pair production in association with two hard jets at the LHC.

2.1 General setup

The hadronic production of two oppositely charged leptons and two hard jets $\text{pp} \to \text{jj}\ell^-\ell^+$ proceeds via the partonic subprocesses

$$q_i\,\text{g} \to q_i\,\text{g}\,\ell^-\,\ell^+, \tag{2.1}$$

$$q_i\,q_j \to q_i\,q_j\,\ell^-\,\ell^+, \qquad q_i, q_j = \text{u}, \text{c}, \text{d}, \text{s}, \text{b} \tag{2.2}$$

and their crossing-related counterparts. Since we neglect flavour mixing as well as the masses of light quarks $(\text{u}, \text{c}, \text{d}, \text{s}, \text{b})$, the LO amplitudes do not depend on the quark generation, and the contributions of the various generations to the cross section differ only by their parton luminosities. All partonic processes can be constructed from the six basic channels $\text{ug} \to \text{ug}\,\ell^-\ell^+$, $\text{dg} \to \text{dg}\,\ell^-\ell^+$, $\text{us} \to \text{us}\,\ell^-\ell^+$, $\text{uc} \to \text{uc}\,\ell^-\ell^+$, $\text{ds} \to \text{ds}\,\ell^-\ell^+$, and $\text{us} \to \text{dc}\,\ell^-\ell^+$ via crossing symmetry and combination. While the mixed quark–gluon (gluonic) channels (2.1) contribute to the cross section exclusively at order $\mathcal{O}(\alpha^2\alpha_\text{s}^2)$, the four-quark channels (2.2) develop LO diagrams of strong as well as of EW nature leading to contributions of order $\mathcal{O}(\alpha^2\alpha_\text{s}^2)$, $\mathcal{O}(\alpha^3\alpha_\text{s})$, and $\mathcal{O}(\alpha^4)$

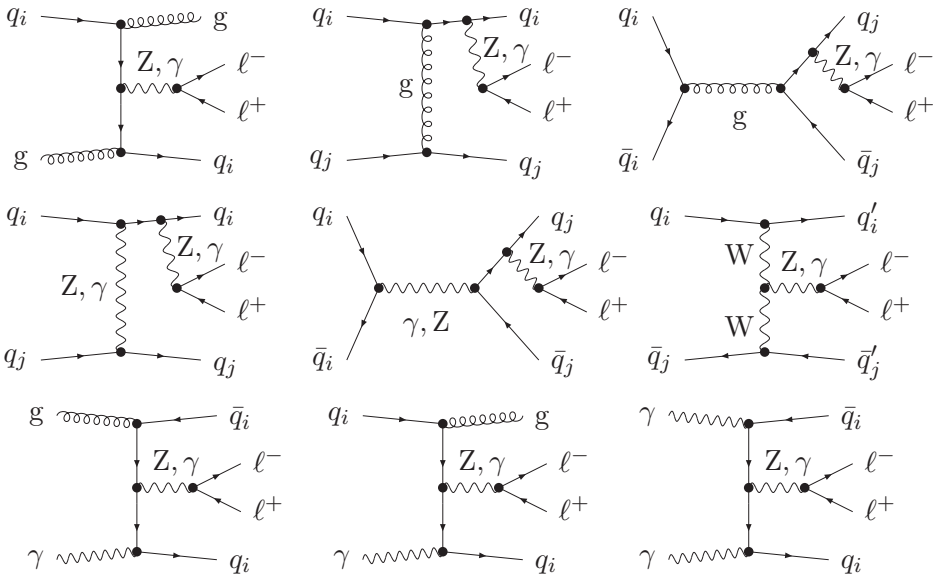

Figure 1: Sample tree diagrams for the QCD contributions to $q_i\,\mathrm{g} \to q_i\,\mathrm{g}\,\ell^-\,\ell^+$, $q_i\,q_j \to q_i\,q_j\,\ell^-\,\ell^+$, and $q_i\,\bar{q}_i \to q_j\,\bar{q}_j\,\ell^-\,\ell^+$ (first line) the EW contributions to $q_i\,q_j \to q_i\,q_j\,\ell^-\,\ell^+$, $q_i\,\bar{q}_i \to q_j\,\bar{q}_j\,\ell^-\,\ell^+$ and $q_i\,\bar{q}_j \to q_i'\,\bar{q}_j'\,\ell^-\,\ell^+$ (second line) and the contributions to $\mathrm{g}\,\gamma \to \bar{q}_i\,q_i\,\ell^-\,\ell^+$, $q_i\,\gamma \to q_i\,\mathrm{g}\,\ell^-\,\ell^+$ and $\gamma\,\gamma \to q_i\,\bar{q}_i\,\ell^-\,\ell^+$.

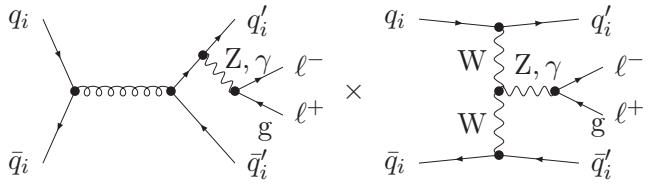

Figure 2: Sample tree diagrams for interferences of QCD and EW diagrams.

to the cross section (see Fig. 1 first two lines for sample diagrams). Owing to the colour structure, nonzero contributions of $\mathcal{O}(\alpha^3\alpha_\mathrm{s})$ only appear in interferences between diagrams with different fermion number flow, and therefore only in partonic channels with identical or weak-isospin-partner quarks (see Fig. 2 for an example). Additional contributions arise from photon-induced production mechanisms

$$\begin{aligned}
\mathrm{g}\,\gamma &\to q_i\,\bar{q}_i\,\ell^-\,\ell^+,\\
q_i\,\gamma &\to q_i\,\mathrm{g}\,\ell^-\,\ell^+,\\
\bar{q}_i\,\gamma &\to \bar{q}_i\,\mathrm{g}\,\ell^-\,\ell^+,\\
\gamma\,\gamma &\to q_i\,\bar{q}_i\,\ell^-\,\ell^+
\end{aligned} \tag{2.3}$$

(see Fig. 1 last line for sample diagrams).

For the calculation of the differential cross section at LO and NLO we follow closely the implementation of $\mathrm{Z} + 2\,\mathrm{jet}$ production in Ref. [14]. Potentially resonant Z-boson propagators are described attributing a complex mass

$$\mu_\mathrm{Z}^2 = M_\mathrm{Z}^2 - \mathrm{i}M_\mathrm{Z}\Gamma_\mathrm{Z}. \tag{2.4}$$

To this end we consistently use the complex-mass scheme [37–39] where μ_W^2 and μ_Z^2 are defined as the poles of the W- and Z-boson propagators in the complex plane. The pole values M_V

and Γ_V ($V = \mathrm{W}, \mathrm{Z}$) for the mass and width of the W and Z boson are related to the on-shell quantities M_V^{OS} and Γ_V^{OS} obtained from the LEP and Tevatron experiments by [40]

$$M_V = M_V^{\mathrm{OS}}/\sqrt{1+(\Gamma_V^{\mathrm{OS}}/M_V^{\mathrm{OS}})^2}\,, \qquad \Gamma_V = \Gamma_V^{\mathrm{OS}}/\sqrt{1+(\Gamma_V^{\mathrm{OS}}/M_V^{\mathrm{OS}})^2}\,. \tag{2.5}$$

We define the electromagnetic coupling constant α within the G_μ scheme, i.e. we fix the value of α via its tree-level relation with the Fermi constant G_μ:

$$\alpha_{G_\mu} = \frac{\sqrt{2} G_\mu M_{\mathrm{W}}^2}{\pi}\left(1 - \frac{M_{\mathrm{W}}^2}{M_{\mathrm{Z}}^2}\right). \tag{2.6}$$

Compared to the Thomson-limit definition of α, (2.6) incorporates effects of the renormalisation-group running from the scale $Q^2 = 0$ to the scale $Q^2 = M_{\mathrm{W}}^2$. Moreover, using (2.6) the renormalisation of α becomes independent of light quark masses and the hadronic vacuum polarisation.

For the analysis we use the following numerical input parameters [41, 42]:

$$\begin{aligned}
G_\mu &= 1.1663787 \times 10^{-5}\,\mathrm{GeV}^{-2}, & & \\
M_{\mathrm{W}}^{\mathrm{OS}} &= 80.385\,\mathrm{GeV}, & \Gamma_{\mathrm{W}}^{\mathrm{OS}} &= 2.085\,\mathrm{GeV}, \\
M_{\mathrm{Z}}^{\mathrm{OS}} &= 91.1876\,\mathrm{GeV}, & \Gamma_{\mathrm{Z}}^{\mathrm{OS}} &= 2.4952\,\mathrm{GeV}, \\
M_{\mathrm{H}} &= 125\,\mathrm{GeV}, & m_{\mathrm{t}} &= 173.2\,\mathrm{GeV}.
\end{aligned} \tag{2.7}$$

The superscript OS denotes on-shell values, and the corresponding pole masses and widths entering our calculation are obtained by (2.5).

We are mainly interested in the relative size of the $\mathcal{O}(\alpha_s^2\alpha^3)$ corrections compared to the LO prediction, which is dominated by $\mathcal{O}(\alpha_s^2\alpha^2)$ contributions. In the corresponding ratio α_s enters exclusively through subdominant contributions to the LO quark channels and any α_s dependence is thus strongly suppressed. Since we do not include the leading QCD corrections, we resort to LO parton distribution functions (PDFs) using, if not stated otherwise, the LHAPDF implementation of the central MSTW2008LO PDF set [43]. From there we infer the value of the strong coupling constant to

$$\alpha_{\mathrm{s}}^{\mathrm{LO}}(M_{\mathrm{Z}}) = 0.139395\ldots\,. \tag{2.8}$$

We choose the QCD factorisation scale μ_{F} and the renormalisation scale μ_{R} as

$$\mu_{\mathrm{F}} = \mu_{\mathrm{R}} = M_{\mathrm{Z}}\,. \tag{2.9}$$

The considered relative corrections depend only weakly on these scales.

For the jet-reconstruction we use the anti-k_{T} clustering algorithm [44] with separation parameter $R = 0.4$. The spatial distance between partons i and j, $\Delta R_{ij} = \sqrt{(y_i - y_j)^2 + (\phi_i - \phi_j)^2}$, is defined in terms of rapidity $y = \frac{1}{2}\ln[(E + p_{\mathrm{L}})/(E - p_{\mathrm{L}})]$, where p_{L} is the momentum component along the beam axis, and azimuthal angle ϕ of the partons. Only partons with $|y_i| < 5$ are clustered. We include also photons and leptons in the jet clustering according to the anti-k_{T} description with $R = 0.4$. While quarks and/or gluons are combined into jets, leptons and photons are recombined into leptons, and quarks/gluons and photons are combined into jets.

We apply two different sets of phase-space cuts to define the production cross section. The first set is inspired by an ATLAS analysis [21] for the production of jets in association with a Z boson at $\sqrt{s} = 7\,\mathrm{TeV}$. The second set of cuts constitutes a typical vector-boson-fusion (VBF) setup, i.e. similar cuts are usually applied in order to enhance in Hjj signatures the production channel via vector-boson-fusion production.

Denoting the momenta of the incoming partons by k_1, k_2 and the final-state momenta by $k_i = \{k_{\mathrm{j}_1}, k_{\mathrm{j}_2}, k_{\ell^-}, k_{\ell^+}\}$, the LO cross section σ_{LO} is obtained as

$$\sigma_{\mathrm{LO}} = \frac{1}{2k_1k_2} \int \mathrm{d}\mathcal{P}(x_i) \int \mathrm{d}\Phi(k_i)\, \Theta_{\mathrm{cut}}(k_i)\, |\mathcal{M}_{\mathrm{LO}}(k_1, k_2, k_i)|^2, \tag{2.10}$$

where $\mathrm{d}\mathcal{P}(x_i)$ incorporates the convolution with the parton distributions functions, $\mathrm{d}\Phi(k_i)$ represents the phase space measure, and $\Theta_{\mathrm{cut}}(k_i)$ defines the acceptance function.

2.2 The pole approximation

We also consider the LO total cross section in the pole approximation $\mathrm{pp} \to \mathrm{jjZ} \to \mathrm{jj}\ell^+\ell^-$. From the full LO amplitude $\mathcal{M}_{\mathrm{LO}}$ we define the subamplitude $\mathcal{M}^{\mathrm{Z}}_{\mathrm{LO}}$ where only diagrams corresponding to the production of a Z boson and its subsequent leptonic decay are taken into account and all non-resonant diagrams (including those with a virtual photon decaying into a lepton pair) are neglected. While the phase space is populated with lepton momenta k_{ℓ^-}, k_{ℓ^+} of generic invariant mass $M^2_{\ell^-\ell^+} = (k_{\ell^-} + k_{\ell^+})^2$, the matrix element $\mathcal{M}^{\mathrm{Z}}_{\mathrm{LO}}$ is calculated with on-shell-projected momenta, i.e. momenta where the invariant mass of the lepton pair equals exactly the Z-boson mass. Only the resonant Z-boson propagator is replaced by its off-shell variant by means of a correcting prefactor. The LO cross section $\sigma^{\mathrm{Z}}_{\mathrm{LO}}$ in the pole approximation thus reads

$$\sigma^{\mathrm{Z}}_{\mathrm{LO}} = \frac{1}{2k_1k_2} \int \mathrm{d}\mathcal{P}(x_i) \int \mathrm{d}\Phi(k_i)\, \Theta_{\mathrm{cut}}(k_i) \left|\frac{M_{\mathrm{Z}}\Gamma_{\mathrm{Z}}}{k^2_{\mathrm{Z}} - M^2_{\mathrm{Z}} - \mathrm{i}M_{\mathrm{Z}}\Gamma_{\mathrm{Z}}}\right|^2 \left|\mathcal{M}^{\mathrm{Z}}_{\mathrm{LO}}(k_1, k_2, \tilde{k}_i)\right|^2, \tag{2.11}$$

where

$$k_{\mathrm{Z}} = k_{\ell^-} + k_{\ell^+}. \tag{2.12}$$

The on-shell projected final-state momenta $\tilde{k}_i$ are constructed from the off-shell momenta k_i through

$$\begin{aligned}
\tilde{k}_{\mathrm{j}_1} &= \beta k_{\mathrm{j}_1}, \qquad \tilde{k}_{\mathrm{j}_2} = \beta k_{\mathrm{j}_2}, \\
\tilde{k}_{\mathrm{Z}} &= k_{\mathrm{Z}} + (1-\beta)(k_{\mathrm{j}_1} + k_{\mathrm{j}_2}), \\
\tilde{k}_{\ell^-} &= \frac{M^2_{\mathrm{Z}}}{2(\tilde{k}_{\mathrm{Z}} k_{\ell^-})} k_{\ell^-}, \qquad \tilde{k}_{\ell^+} = \tilde{k}_{\mathrm{Z}} - \tilde{k}_{\ell^-},
\end{aligned} \tag{2.13}$$

where β is chosen in such a way that $\tilde{k}^2_{\mathrm{Z}} = M^2_{\mathrm{Z}}$. Of the two solutions of the quadratic equation

$$\begin{aligned}
0 &= \tilde{k}^2_{\mathrm{Z}} - M^2_{\mathrm{Z}} \\
&= 2(k_{\mathrm{j}_1}k_{\mathrm{j}_2})\beta^2 - [4(k_{\mathrm{j}_1}k_{\mathrm{j}_2}) + 2(k_{\mathrm{j}_1}k_{\mathrm{Z}}) + 2(k_{\mathrm{j}_2}k_{\mathrm{Z}})]\beta \\
&\quad + 2(k_{\mathrm{j}_1}k_{\mathrm{j}_2}) + 2(k_{\mathrm{j}_1}k_{\mathrm{Z}}) + 2(k_{\mathrm{j}_2}k_{\mathrm{Z}}) + k^2_{\mathrm{Z}} - M^2_{\mathrm{Z}}
\end{aligned} \tag{2.14}$$

β is the one closer to 1.

2.3 Leading-order analysis with standard acceptance cuts

In this section we investigate the production of $\mathrm{pp} \to \mathrm{jj}\ell^-\ell^+$, where $\ell = \mathrm{e}$ or μ (not summed), at LO for a set of standard acceptance cuts (called *basic cuts* in the following). We require two hard jets with

$$p_{\mathrm{T,j}} > 30\,\mathrm{GeV}, \qquad |y_{\mathrm{j}}| < 4.5 \tag{2.15}$$

for the transverse momenta p_T and rapidities y and two hard leptons with

$$p_{T,\ell} > 20\,\text{GeV}, \qquad |y_\ell| < 2.5. \tag{2.16}$$

We then apply to the two jets (at NLO to the two or three jets) and the two charged leptons passing the cuts (2.15) and (2.16) the rapidity–azimuthal angle separation cuts

$$\Delta R_{\ell^-\ell^+} > 0.2, \qquad \Delta R_{\ell j} > 0.5, \tag{2.17}$$

and finally a cut on the invariant mass of the lepton pair

$$66\,\text{GeV} < M_{\ell^-\ell^+} < 116\,\text{GeV}. \tag{2.18}$$

The total cross section for the 13 TeV LHC and the set of cuts listed above can be found in Table 1, where it is split into various contributions. Neglecting photon-induced contributions we find

$$\sigma_{\text{tot}}^{13\,\text{TeV}} = 51.209(8)\,\text{pb}. \tag{2.19}$$

We note that about 80% of $jj\ell^-\ell^+$ events will be produced in parton interactions involving external gluons. This is true for the full LO calculation shown in the second column as well as for the pole approximation shown in the third column of Table 1. On average the pole approximation underestimates the size of the cross section for the various processes by 1.5%, in agreement with the expected accuracy of order Γ_Z/M_Z given the cut on $M_{\ell^-\ell^+}$. In addition, Table 1 shows the composition of the total cross section for different partonic processes in terms of the various orders in the strong and the electromagnetic coupling constant. By far the most dominant contribution results from quark–gluon initiated processes, due to the high quark–gluon luminosities in proton–proton collisions. The dominant production mechanism for four-quark processes is given by strong interactions between initial-state partons and jets [$\mathcal{O}(\alpha_s^2\alpha^2)$]. The relative contribution at $\mathcal{O}(\alpha^4)$ varies between a few per mille and a few per cent, except for the process class $u\bar{u} \to d\bar{d}\ell^-\ell^+$. Since t-channel gluon exchange does not contribute in this process class, the absolute contribution is small, but the relative contribution of the EW diagrams (involving t-channel W-boson exchange) is enhanced. Interferences between strong and EW amplitudes [$\mathcal{O}(\alpha_s\alpha^3)$] are comparable to $\mathcal{O}(\alpha^4)$ contributions in absolute size. Since they are not positive definite they lower the cross section slightly for certain partonic processes. As a consequence there are cancellations between different partonic processes, and the relative contribution of $\mathcal{O}(\alpha_s\alpha^3)$ to the total cross section is less than one per mille in our set-up. Partonic processes with external bottom quarks contribute 8.5% to the total cross section.

Before we turn to differential distributions we elaborate on the impact of photon-induced reactions [see (2.3)]. For that purpose we have redone our LO analysis for the LHC operating at 13 TeV employing the NNPDF 2.3 [45] parton distribution functions, using the same input parameters and phase-space cuts as before. With this setup we find the relative contribution of photonic processes to the total cross section to be less than 0.5‰. Assuming that this represents the order of magnitude for photon-induced processes, we neglect these contributions in the following.

In Fig. 3 we present LO differential distributions for the transverse momenta of the hardest jet p_{T,j_1} (jet with highest transverse momentum), the negatively charged lepton p_{T,ℓ^-}, and the lepton pair $p_{T,\ell^-\ell^+}$, as well as the di-jet invariant mass M_{jj}, the scalar sum of all transverse momenta

$$H_T = p_{T,j_1} + p_{T,j_2} + p_{T,\ell^-} + p_{T,\ell^+}, \tag{2.20}$$

process class	σ [fb]	σ^{Z} [fb]	$\sigma/\sigma_{\mathrm{tot}}$ [%]	$\sigma_{\alpha_s^2\alpha^2}/\sigma$ [%]	$\sigma_{\alpha_s\alpha^3}/\sigma$ [%]	σ_{α^4}/σ [%]
$ug \to ug\ell^-\ell^+$, $dg \to dg\ell^-\ell^+$ $\bar{u}g \to \bar{u}g\ell^-\ell^+$, $\bar{d}g \to \bar{d}g\ell^-\ell^+$	34584(8)	34105(10)	67.5	100	—	—
$u\bar{u} \to gg\ell^-\ell^+$, $d\bar{d} \to gg\ell^-\ell^+$	2713(1)	2671(1)	5.3	100	—	—
$gg \to u\bar{u}\ell^-\ell^+$, $gg \to d\bar{d}\ell^-\ell^+$	3612(1)	3574(1)	7.1	100	—	—
$uu \to uu\ell^-\ell^+$, $dd \to dd\ell^-\ell^+$ $\bar{u}\bar{u} \to \bar{u}\bar{u}\ell^-\ell^+$, $\bar{d}\bar{d} \to \bar{d}\bar{d}\ell^-\ell^+$	1315.1(3)	1291.4(4)	2.6	97.4	+2.0	0.5
$u\bar{u} \to u'\bar{u}'\ell^-\ell^+$, $d\bar{d} \to d'\bar{d}'\ell^-\ell^+$ $u\bar{u}' \to u\bar{u}'\ell^-\ell^+$, $d\bar{d}' \to d\bar{d}'\ell^-\ell^+$ $u\bar{u} \to u\bar{u}\ell^-\ell^+$, $d\bar{d} \to d\bar{d}\ell^-\ell^+$	2463.7(5)	2420.5(7)	4.8	98.3	−1.3	2.9
$u\bar{u} \to d\bar{d}\ell^-\ell^+$, $d\bar{d} \to u\bar{u}\ell^-\ell^+$ $u\bar{u}' \to d\bar{d}'\ell^-\ell^+$, $d\bar{d}' \to u\bar{u}'\ell^-\ell^+$	438.82(7)	432.6(1)	0.9	76.6	−9.0	32.3
$ud \to u'd'\ell^-\ell^+$, $\bar{u}\bar{d} \to \bar{u}'\bar{d}'\ell^-\ell^+$ $ud \to ud\ell^-\ell^+$, $\bar{u}\bar{d} \to \bar{u}\bar{d}\ell^-\ell^+$ $uu' \to uu'\ell^-\ell^+$, $\bar{u}\bar{u}' \to \bar{u}\bar{u}'\ell^-\ell^+$ $dd' \to dd'\ell^-\ell^+$, $\bar{d}\bar{d}' \to \bar{d}\bar{d}'\ell^-\ell^+$	3856.8(7)	3800(1)	7.5	92.9	+2.8	4.3
$u\bar{d} \to u'\bar{d}'\ell^-\ell^+$, $\bar{u}d \to \bar{u}'d'\ell^-\ell^+$ $u\bar{d} \to u\bar{d}\ell^-\ell^+$, $\bar{u}d \to \bar{u}d\ell^-\ell^+$	2224.9(4)	2197.1(6)	4.3	95.9	−1.1	5.2
gluonic	40910(8)	40349(11)	79.9	100	—	—
four-quark	10299(1)	10141(1)	20.1	94.7	+0.4	4.8
bottom quarks	4376(3)	—	8.54	—	—	—
sum	51209(8)	50490(11)	100	98.9	< 0.1	1.0

Table 1: Composition of the LO cross section for $pp \to jj\ell^-\ell^+$ at the LHC operating at 13 TeV for basic cuts. In the first column the contributing partonic processes are listed, where $u, u' \neq u$ denote the up-type quarks u, c and $d, d' \neq d$ the down-type quarks d, s, b. The second column provides the corresponding cross section where the numbers in parenthesis give the integration error on the last digit. The cross section for the pole approximation is given in the third column. The fourth column contains the relative contribution to the total cross section in per cent. In the fifth, sixth and seventh column we provide the relative contribution to a partonic channel from strong and EW contributions and their interference.

and the relative azimuthal angle $\phi_{\ell^-\ell^+}$ between the two leptons. The upper panels depict the absolute distributions at leading order. In the middle panels we illustrate the composition of these distributions in terms of gluonic (red, short-dashed) and four-quark (blue, long-dashed) processes including all light flavours (u, d, s, c, b) and show the relevance of processes involving at least one external bottom quark (magenta, dashed-dotted). In the lower panels we present the relative contributions of the squared EW diagrams (purple, dotted) and the QCD–EW interference (orange, long-dashed dotted). The distribution of the transverse momentum of the hardest jet (upper left plot of Fig. 3) drops by about six orders of magnitude in the depicted range $p_{\mathrm{T,j_1}} \leq 2\,\mathrm{TeV}$. The composition of the distribution changes significantly with increasing $p_{\mathrm{T,j_1}}$. For low transverse momentum, gluonic processes dominate while for higher $p_{\mathrm{T,j_1}}$ values the four-quark processes become more important and dominate for $p_{\mathrm{T,j_1}} \gtrsim 1100\,\mathrm{GeV}$. We find a similar composition for other jet observables which are energy dependent like the transverse momentum distribution of the second hardest jet (not shown) or the invariant jet mass of the two hardest jets (upper right plot of Fig. 3). This behaviour is reminiscent of the relative gluon and quark-induced contributions in di-jet production [46, 47] and is related to the different characteristics of quark and gluon parton distribution functions. We have checked that the events with high $p_{\mathrm{T,j_1}}$ are dominated by events with two hard jets and relatively soft leptons.

We consider the differential cross section as a function of the transverse momentum of the negatively charged lepton in the middle left plot of Fig. 3. The distribution shows a drop over seven orders of magnitude for $20\,\mathrm{GeV} < p_{\mathrm{T},\ell^-} < 1500\,\mathrm{GeV}$. Since the leptons result mainly from Z-boson decays their transverse-momentum distributions show a stronger drop compared to those of the jets, which are produced directly in the collision. Events with high p_{T,ℓ^-} are typically accompanied by a hard jet balancing the transverse momentum and a soft jet. It is striking that the relative composition of this distribution in terms of gluonic and four-quark contributions is largely independent of p_{T,ℓ^-}. For any p_{T,ℓ^-} value, about three quarters of the $\mathrm{pp} \to \mathrm{jj}\ell^-\ell^+$ events are produced in interactions involving external gluons. For the distributions in the transverse momentum of the positively charged lepton (not shown) and the lepton pair (middle right plot of Fig. 3) we find similar results.

The lower left plot of Fig. 3 depicts the H_{T} distribution, which is sensitive to both, lepton and jet transverse momenta. With increasing H_{T} the relative contributions behave similarly as for the p_{T,j_1} distribution. Four-quark and gluonic contributions break even around $H_{\mathrm{T}} = 2300\,\mathrm{GeV}$. Finally, we consider the azimuthal angle between the leptons. We find that the two leptons prefer to be anticollinear in the transverse plane. This comes about as the lepton pairs result mainly from the decays of relatively soft Z bosons. We observe a rather constant ratio between gluonic and four-quark processes as a function of $\phi_{\ell^-\ell^+}$.

We note that partonic contributions involving external bottom quarks have only a minor impact in all studied differential distributions. They are below ten per cent in all cases and even much smaller in the high-energy tails of the distributions.

While the EW contributions stay at the level of 1% in the $p_{\mathrm{T,j_1}}$ distribution, they increase with M_{jj}, reaching almost 20% at $M_{\mathrm{jj}} = 5\,\mathrm{TeV}$. The QCD–EW interference grows to 10% for $p_{\mathrm{T,j_1}} = 2\,\mathrm{TeV}$. While the EW contributions are generally small for other distributions, a sizable QCD–EW interference is also visible in the H_{T} distribution reaching 10% at 4 TeV (lower left plot of Fig. 3). For distributions in lepton variables and for rapidity distributions of jets, both EW contributions and QCD–EW interferences are below one per cent. EW contributions are larger for large rapidity or rapidity–azimuthal-angle separation of the jets.

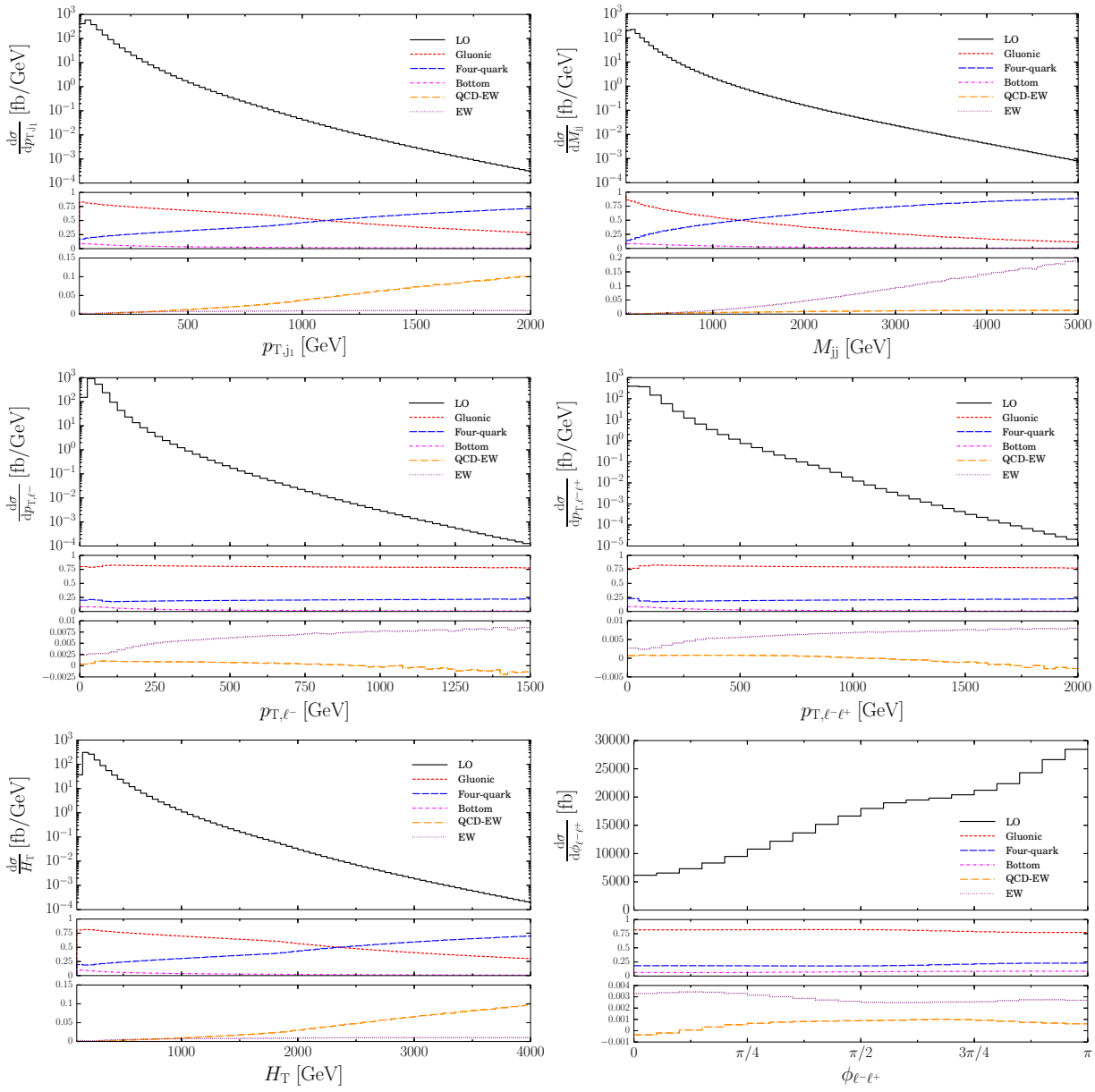

Figure 3: Distributions of the transverse momentum of the harder jet j_1, the di-jet invariant mass M_{jj}, the transverse momenta of the negatively charged lepton ℓ^- and the lepton pair $\ell^-\ell^+$, the scalar sum of all transverse momenta, and the relative azimuthal angle between the leptons at the 13 TeV LHC for basic cuts. The upper panels show the corresponding distributions, the middle ones the composition of the cross section and the lower ones the contributions of the EW diagrams. Further details are described in the text.

2.4 Leading-order analysis with VBF cuts

We now examine the LO cross section for the process $pp \to jj\ell^-\ell^+$ using the same input parameters as in the previous section and employing the cuts (2.15), (2.16), (2.17) as before, but instead of (2.18) the following VBF cuts

$$\begin{aligned} &M_{jj} > 600\,\text{GeV}, \quad |y_{j_1} - y_{j_2}| > 4, \quad y_{j_1} \cdot y_{j_2} < 0, \\ &\min(y_{j_1}, y_{j_2}) < y_\ell < \max(y_{j_1}, y_{j_2}). \end{aligned} \tag{2.21}$$

Here j_1 and j_2 are the leading and subleading jets, i.e. the jets with the highest transverse momenta.

The results for the cross section with VBF cuts are given in Table 2. Compared with the result for standard acceptance cuts in (2.19) the total cross section decreased by a factor of 50. This reduction of the signal is a result of the strong VBF constraints to the phase space. While gluonic processes still dominate the cross section their relative contribution decreased to 59%. The pole approximation does not work as well as in the previous setup and underestimates the full result at LO by about 11%. This is due to the fact that we did not apply the cut (2.18) thus allowing for a larger contribution from photon exchanges. When imposing the cut (2.18) in the VBF set-up, the pole approximation is again accurate at the level of 1−2 per cent. The EW contributions of $\mathcal{O}(\alpha^4)$ become more significant (17% in the four-quark processes and 7% in the total sum), while interferences between EW and QCD amplitudes are below 1% for all four-quark processes for this setup apart from the suppressed channels of type $u\bar{u} \to d\bar{d}\ell^-\ell^+$.

The corresponding differential distributions are shown in Fig. 4. For the transverse momentum distributions of the hardest jet, the negatively charged lepton and the lepton pair as well as for the H_T distribution we find no significant qualitative changes beside the reduced normalisation. The distribution in the di-jet invariant mass decreases much slower as events with large M_{jj} tend to pass VBF cuts. The variation in the $\phi_{\ell^-\ell^+}$ distribution is smaller than for basic cuts. However, VBF kinematics also affects the composition of the distributions. For the p_{T,j_1} distribution the relative gluonic contribution drops from 60% at $p_{T,j_1} = 30\,\text{GeV}$ below 50% at $p_{T,j_1} = 270\,\text{GeV}$. This is in line with the fact that VBF cuts tend to enhance the four-quark contributions. The resulting balance between four-quark and gluonic contributions is valid for higher transverse momenta up to 1 TeV. Thus for large p_{T,j_1} the four-quark contributions are less relevant as for basic cuts. The composition of the distribution in the di-jet invariant mass is very similar as for basic cuts. For large p_{T,ℓ^-} or large $p_{T,\ell^-\ell^+}$ four-quark and gluonic contributions are about equal. In the case of the H_T distribution we find gluonic and four-quark contributions similar as for the p_{T,j_1} distribution. The composition does hardly depend on the azimuthal angle between the leptons $\phi_{\ell^-\ell^+}$. As for basic cuts, the EW diagrams contribute sizeably (50% for $M_{jj} = 5\,\text{TeV}$) for large M_{jj} (as well as large Δy_{jj} or ΔR_{jj}), while they stay at the level of 10% for other distributions. QCD–EW interferences (multiplied by a factor 10 in Fig. 4) are at the per-mille level for all considered distributions in the VBF set-up.

The relative contribution of bottom quarks is always below 5% and drops to the per-mille level in the high-energy tails of distributions.

3 NLO electroweak corrections to $pp \to jj\ell^-\ell^+$

3.1 General remarks

In this section we consider NLO electroweak corrections to the process $pp \to jj\ell^-\ell^+$. Since the dominant contributions in LO perturbation theory are of $\mathcal{O}(\alpha_s^2\alpha^2)$ we focus on electroweak

process class	σ [fb]	σ^{Z} [fb]	$\sigma/\sigma_{\mathrm{tot}}$ [%]	$\sigma_{\alpha_{\mathrm{s}}^2\alpha^2}/\sigma$ [%]	$\sigma_{\alpha_{\mathrm{s}}\alpha^3}/\sigma$ [%]	σ_{α^4}/σ [%]
$ug \to ug\ell^-\ell^+$, $dg \to dg\ell^-\ell^+$ $\bar{u}g \to \bar{u}g\ell^-\ell^+$, $\bar{d}g \to \bar{d}g\ell^-\ell^+$	540.9(3)	482.4(3)	52.0	100	—	—
$u\bar{u} \to gg\ell^-\ell^+$, $d\bar{d} \to gg\ell^-\ell^+$	22.35(1)	19.80(1)	2.2	100	—	—
$gg \to u\bar{u}\ell^-\ell^+$, $gg \to d\bar{d}\ell^-\ell^+$	54.53(4)	50.56(3)	5.2	100	—	—
$uu \to uu\ell^-\ell^+$, $dd \to dd\ell^-\ell^+$ $\bar{u}\bar{u} \to \bar{u}\bar{u}\ell^-\ell^+$, $\bar{d}\bar{d} \to \bar{d}\bar{d}\ell^-\ell^+$	86.22(5)	73.70(5)	8.3	97.0	0.1	2.8
$u\bar{u} \to u'\bar{u}'\ell^-\ell^+$, $d\bar{d} \to d'\bar{d}'\ell^-\ell^+$ $u\bar{u}' \to u\bar{u}'\ell^-\ell^+$, $d\bar{d}' \to d\bar{d}'\ell^-\ell^+$ $u\bar{u} \to u\bar{u}\ell^-\ell^+$, $d\bar{d} \to d\bar{d}\ell^-\ell^+$	65.98(3)	57.64(3)	6.3	98.2	-0.1	2.0
$u\bar{u} \to d\bar{d}\ell^-\ell^+$, $d\bar{d} \to u\bar{u}\ell^-\ell^+$ $u\bar{u}' \to d\bar{d}'\ell^-\ell^+$, $d\bar{d}' \to u\bar{u}'\ell^-\ell^+$	21.198(7)	20.102(7)	2.0	1.9	-4.6	102.7
$ud \to u'd'\ell^-\ell^+$, $\bar{u}\bar{d} \to \bar{u}'\bar{d}'\ell^-\ell^+$ $ud \to ud\ell^-\ell^+$, $\bar{u}\bar{d} \to \bar{u}\bar{d}\ell^-\ell^+$ $uu' \to uu'\ell^-\ell^+$, $\bar{u}\bar{u}' \to \bar{u}\bar{u}'\ell^-\ell^+$ $dd' \to dd'\ell^-\ell^+$, $\bar{d}\bar{d}' \to \bar{d}\bar{d}'\ell^-\ell^+$	180.61(8)	163.94(8)	17.3	74.0	1.1	24.9
$u\bar{d} \to u'\bar{d}'\ell^-\ell^+$, $\bar{u}d \to \bar{u}'d'\ell^-\ell^+$ $u\bar{d} \to u\bar{d}\ell^-\ell^+$, $\bar{u}d \to \bar{u}d\ell^-\ell^+$	67.73(3)	61.01(3)	6.5	99.0	-0.1	1.1
gluonic	617.8(4)	552.8(3)	59.4	100	—	—
four-quark	421.7(1)	376.4(1)	40.6	82.9	0.2	16.9
bottom quarks	51.82(2)	—	4.98	—	—	—
sum	1039.6(4)	929.2(3)	100	93.1	0.01	6.9

Table 2: Composition of the LO cross section for $pp \to jj\ell^-\ell^+$ at the LHC operating at 13 TeV for VBF cuts. In the first column the contributing partonic processes are listed, where $u, u' \neq u$ denote the up-type quarks u, c and $d, d' \neq d$ the down-type quarks d, s, b. The second column provides the corresponding cross section where the numbers in parentheses give the integration error on the last digit. The third column contains the relative contribution to the total cross section in per cent. In the fourth, fifth and sixth column we provide the relative contribution to a partonic channel from strong and EW contributions and their interference.

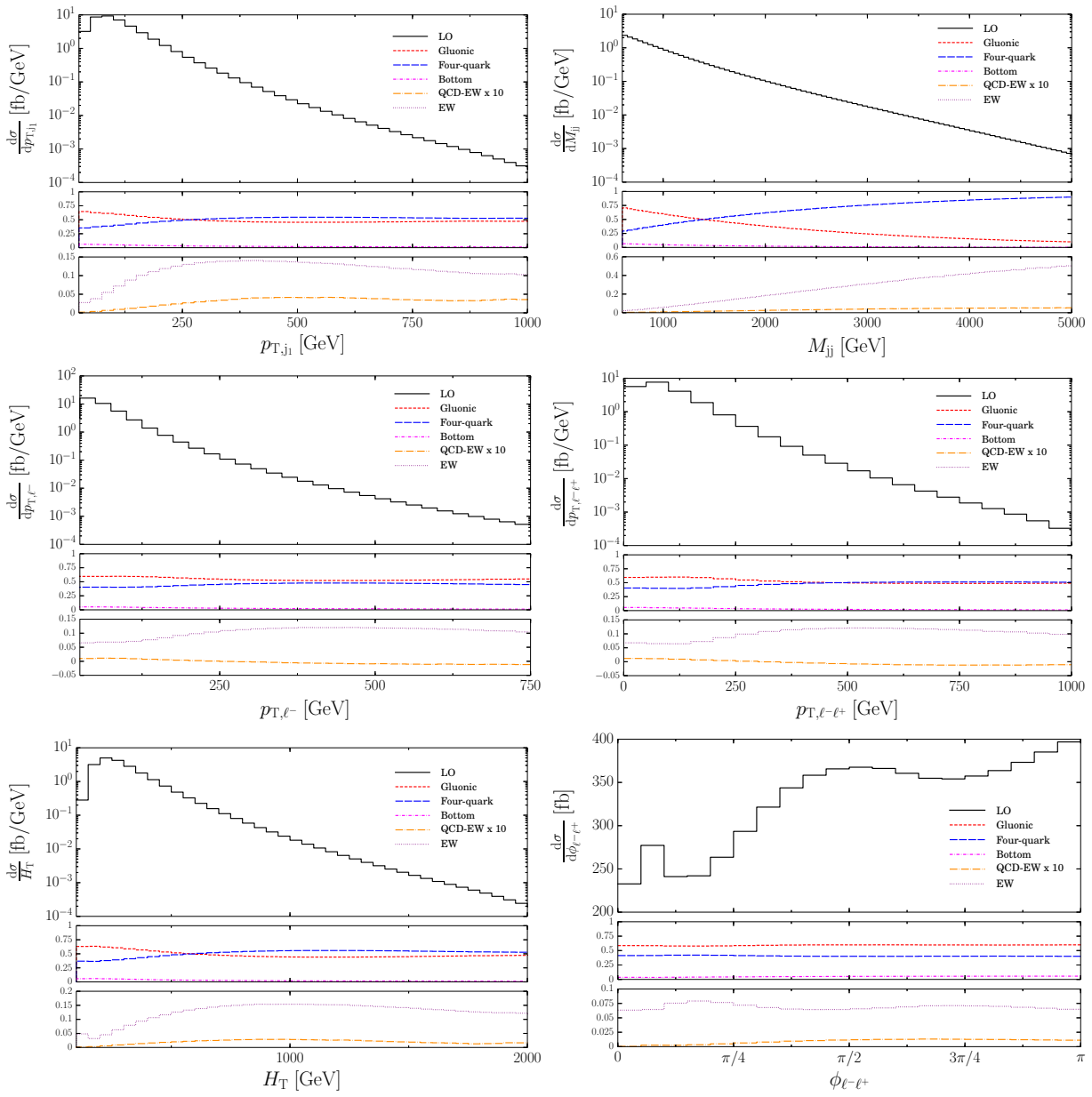

Figure 4: Distributions of the transverse momentum of the harder jet j_1, the di-jet invariant mass M_{jj}, the transverse momenta of the negatively charged lepton ℓ^- and the lepton pair $\ell^-\ell^+$, the scalar sum of all transverse momenta, and the relative azimuthal angle between the leptons at 13 TeV LHC for the VBF setup. The upper panels show the corresponding distributions, the middle ones the composition of the cross section and the lower ones the contributions of the EW diagrams. Further details are described in the text.

corrections to these dominant contributions and study the complete set of $\mathcal{O}(\alpha_s^2\alpha^3)$ contributions. LO gluonic processes contribute exclusively at order $\mathcal{O}(\alpha_s^2\alpha^2)$ requiring the calculation of electroweak $\mathcal{O}(\alpha)$ one-loop corrections and real photon emission

$$\delta\sigma^{\text{NLO,gluonic}}_{\text{pp}\to\text{jj}\ell^-\ell^+} = \delta\sigma^{\text{virtual,gluonic}}_{\text{pp}\to\text{jj}\ell^-\ell^+} + \delta\sigma^{\text{real,gluonic}}_{\text{pp}\to\text{jj}\ell^-\ell^+\gamma}. \tag{3.1}$$

Four-quark processes feature various powers of the electromagnetic and the strong coupling constant at LO and thus the computation is more involved. A complete treatment in perturbation theory at $\mathcal{O}(\alpha_s^2\alpha^3)$ for these processes requires the incorporation of

a) corrections of $\mathcal{O}(\alpha)$ to LO QCD contributions of $\mathcal{O}(\alpha_s^2\alpha^2)$, and

b) corrections of $\mathcal{O}(\alpha_s)$ to LO QCD–EW interferences of $\mathcal{O}(\alpha_s\alpha^3)$.

Consequently, we need to incorporate photon and gluon real emission

$$\delta\sigma^{\text{NLO,four-quark}}_{\text{pp}\to\text{jj}\ell^-\ell^+} = \delta\sigma^{\text{virtual,four-quark}}_{\text{pp}\to\text{jj}\ell^-\ell^+} + \delta\sigma^{\text{real,four-quark}}_{\text{pp}\to\text{jj}\ell^-\ell^+\gamma} + \delta\sigma^{\text{real,four-quark}}_{\text{pp}\to\text{jj}\ell^-\ell^+\text{g}} \tag{3.2}$$

at the relevant order.

Contributions involving external bottom quarks contribute less than 10% to the total cross section and differential distributions, and we do not consider NLO electroweak corrections to these processes.

3.2 Virtual corrections

The virtual amplitudes are calculated using the 't Hooft–Feynman gauge. The amplitudes for the various partonic processes can be constructed from the same basic channels as at LO. Sample diagrams are given in Fig. 5. The virtual electroweak corrections for a gluonic process like $\text{ug}\to\text{ug}\ell^-\ell^+$ involve $\mathcal{O}(1200)$ diagrams, including 18 hexagons and 85 pentagons, all contributing to the cross section at $\mathcal{O}(\alpha_s^2\alpha^3)$. For the $\text{us}\to\text{us}\ell^-\ell^+$ channel there are about 150 diagrams of order $\mathcal{O}(g_s^4e^2)$ (QCD corrections to LO QCD contributions), and some 800 diagrams of order $\mathcal{O}(g_s^2e^4)$, including 32 hexagons and 50 pentagons. At $\mathcal{O}(\alpha_s^2\alpha^3)$ the former contribute via interference with LO EW diagrams, the latter via interference with LO QCD diagrams. Additional diagrams of order $\mathcal{O}(e^6)$, the EW corrections to LO EW diagrams, do not contribute at the considered order. The $\text{us}\to\text{dc}\ell^-\ell^+$ channel furnishes no contributions of order $\mathcal{O}(g_s^4e^2)$ but about 120 diagrams of order $\mathcal{O}(g_s^2e^4)$, including 24 hexagons and 4 pentagons, as well as diagrams of order $\mathcal{O}(e^6)$ that are irrelevant in our approximation.

The most complicated topologies involve 6-point functions up to rank 4. For the calculation of tensor integrals we use the library Collier [17, 18]. It implements the recursive numerical reduction methods of Refs. [48, 49], where numerical instabilities from small Gram determinants are avoided by choosing suitable expansion algorithms depending on the actual input momenta. The scalar integrals are evaluated according to the explicit results of Refs. [50–52]. Both, in the case of ultraviolet divergences as well as in the case of infrared (IR) divergences, dimensional regularisation is applied to extract the corresponding singularities. The EW sector of the SM is renormalised using an on-shell prescription for the W- and Z-boson masses in the framework of the complex-mass scheme [38]. As the coupling α_{G_μ} is derived from M_W, M_Z and G_μ its counterterm inherits a correction term Δr from the weak corrections to muon decay.

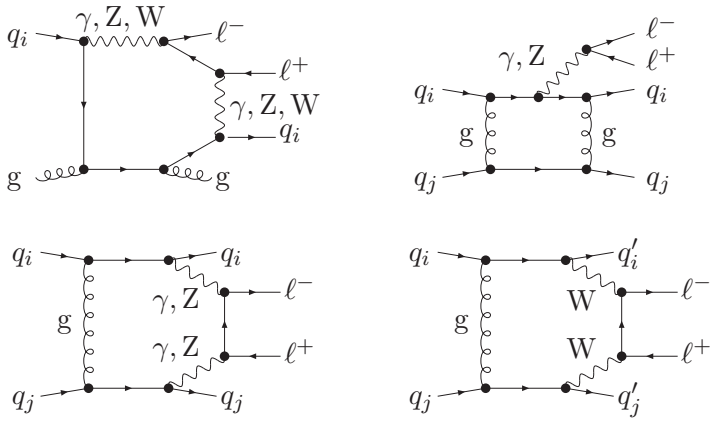

Figure 5: Sample diagrams for virtual corrections: hexagon of $\mathcal{O}(g_\mathrm{s}^2 e^4)$ for $q_i\,\mathrm{g} \to q_i\,\mathrm{g}\,\ell^-\,\ell^+$ (upper left), pentagon of $\mathcal{O}(g_\mathrm{s}^4 e^2)$ for $q_i\,q_j \to q_i\,q_j\,\ell^-\,\ell^+$ (upper right), hexagon of $\mathcal{O}(g_\mathrm{s}^2 e^4)$ for $q_i\,q_j \to q_i\,q_j\,\ell^-\,\ell^+$ (lower left), hexagon of $\mathcal{O}(g_\mathrm{s}^2 e^4)$ for $q_i\,q_j \to q_i'\,q_j'\,\ell^-\,\ell^+$ (lower right).

3.3 Real corrections

3.3.1 Gluonic processes

The real corrections to the gluonic subprocesses are induced by photon Bremsstrahlung (see Fig. 6 left for a sample diagram) and are all of $\mathcal{O}(\alpha_\mathrm{s}^2\alpha^3)$. IR divergences resulting from emission of a soft or a collinear photon from an external quark are regularised dimensionally. For an IR-save event definition, the final-state singularities cancel with corresponding IR poles from the virtual corrections. For the initial-state singularities this cancellation is incomplete but the remnant can be absorbed into a redefinition of the quark distribution function. Technically we make use of the Catani–Seymour dipole formalism [53], with the extension as formulated in Refs. [54–56], which we transferred in a straightforward way to the case of dimensionally regularised photon emission.

In combination with photon radiation also final-state gluons, present in the LO processes, cause IR divergences (see Ref. [34]) when they become soft. While isolated soft gluons do not pass the selection cuts because the requirement of two hard jets is not fulfilled, in IR-safe observables quarks and thus all QCD partons have to be recombined with photons if they are sufficiently collinear. Thus, a soft gluon still passes the selection cuts if it is recombined with a sufficiently hard collinear photon, giving rise to a soft-gluon divergence, which would be cancelled by the virtual QCD corrections to $\mathrm{pp} \to \ell^-\ell^+\mathrm{j}+\gamma$ production. Following Refs. [34, 57] we eliminate this singularity by discarding events which contain a jet consisting of a hard photon recombined with a soft parton a ($a = q_i, \bar{q}_i, \mathrm{g}$): Photonic jets with $z_\gamma = E_\gamma/(E_\gamma + E_a)$ above a critical value z_γ^cut are attributed to the process $\mathrm{pp} \to \ell^-\ell^+\mathrm{j} + \gamma$ and therefore excluded. This event definition is still not IR-save because the application of the z_γ cut to recombined quark–photon jets spoils the cancellation of final-state collinear singularities with the virtual photonic corrections. The left-over singularities can be absorbed into the quark–photon fragmentation function [58, 59]. The additional cut on z_γ implies a modification of the integrated dipole terms. The corresponding expressions and further details can be found in App. A.

In the following numerical analysis, a recombined photon–parton jet is subjected to the cut $z_\gamma = E_\gamma/(E_\gamma + E_a) < 0.7$.

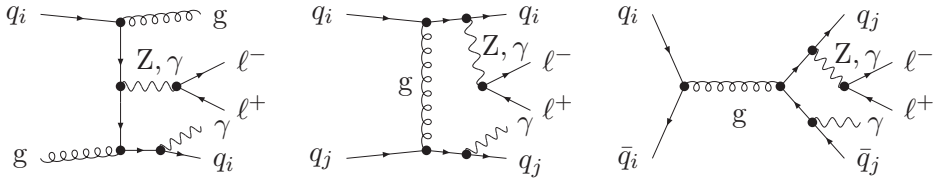

Figure 6: Sample diagrams for real photon radiation: contributions to $q_i\,\mathrm{g} \to q_i\,\mathrm{g}\,\ell^-\,\ell^+\,\gamma$, $q_i\,q_j \to q_i\,q_j\,\ell^-\,\ell^+\,\gamma$ and $q_i\,\bar{q}_i \to q_j\,\bar{q}_j\,\ell^-\,\ell^+\,\gamma$.

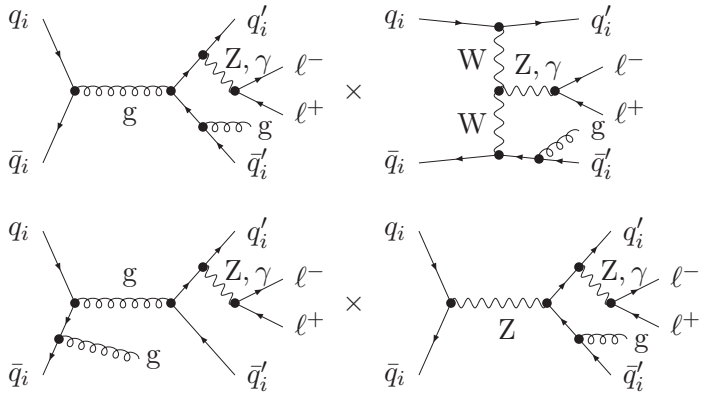

Figure 7: Sample diagrams for interferences of QCD and EW diagrams with gluon radiation.

3.3.2 Four-quark processes

The real corrections to the four-quark processes feature soft and collinear emission of a photon or a gluon. At $\mathcal{O}(\alpha_s^2\alpha^3)$ we have contributions with photon emission from the LO QCD diagrams (see Fig. 6 for examples) and interferences from diagrams with real gluon emission from QCD and EW diagrams (see Fig. 7 for examples). All channels that result from crossing of two quarks or a quark and the gluon have to be taken into account. Crossing the gluon into the initial state leads to partonic subprocesses which do not have a LO counterpart (such as $\mathrm{gu} \to \mathrm{uu\bar{u}}\ell^-\ell^+$) and are IR finite.

In the case of photon emission we employ the same recombination procedure as in the previous subsection and thus ensure the equal treatment of gluons and quarks in the framework of photon fragmentation. For gluon emission amplitudes we apply the standard Catani–Seymour formalism with phase-space restricted subtraction terms [54–56].

3.3.3 Checks

The calculation has been performed with Recola [14,15], which provides all relevant amplitudes for tree level, one loop and real radiation, as well as the colour-correlated squared matrix elements required for the subtraction terms. For the evaluation of the loop integrals Recola uses the tensor-integral library Collier [17, 18]. The phase-space integration is carried out with an in-house multi-channel Monte-Carlo generator [60].

We performed several consistency checks of the calculation. The tensor integrals are evaluated by Collier, which includes a second independent implementation of all its building blocks. We have checked that the cross section and the distributions do not change within integration errors when switching between the different implementations in Collier. Making use of our implementation of phase-space restricted subtraction terms we performed the calculation of all cross sections and distributions both for $\alpha = 1$ and $\alpha = 0.01$ and found agreement within

integration errors. The distributions shown in the following have been obtained with $\alpha = 0.01$, which yields somewhat smoother results.

We have performed various cross-checks of the calculation with conventional methods. To this end we have used FeynArts 3.2 [61, 62], FormCalc 3.1 [3] and Pole [63] for the generation, simplification and calculation of the Feynman amplitudes. The phase-space integration is performed with the multi-channel generator Lusifer [64]. For the gluonic channels a complete second calculation was performed using this second setup in the case of an on-shell Z boson [14]. For the off-shell calculation the individual contributions of real photon emission and the corresponding dipoles and integrated dipoles (including the contribution from photon fragmentation) have been checked against the second implementation taking the channel $ug \to ug\ell^-\ell^+$ as reference. In the case of the four-quark channels, a full integration of the sample channel $ud \to ud\ell^-\ell^+$ has been performed within the second setup yielding perfect agreement with the results (including differential distributions) obtained by Recola.

3.4 Results for standard acceptance cuts

In this section we present NLO results for the total cross section and various differential distributions using the numerical input parameters (2.7) and acceptance cuts (2.15), (2.16), (2.17), and (2.18), as introduced in Section 2.1. In Table 3 we present the impact of the NLO corrections on the various subprocesses. The corrections to the partonic total cross sections are negative for all process classes. Both gluonic and four-quark processes receive rather small relative corrections between -3.1% and -2.2%. They sum up to a correction of -2.5% for the total hadronic cross section. For the LHC operating at 8 TeV we found the total cross section corrected by -2.3% [65].

In Fig. 8 we present the effects of the NLO electroweak corrections on differential distributions. Each plot depicts the correction relative to the LO distribution in per cent. The solid (black) curve represents the ratio of the NLO correction normalised to the LO distribution. Although unphysical we show the impact of real contributions (subtracted real contributions and integrated dipole contributions ignoring the IR poles) from photon (red, long-dashed) and gluon (blue, short-dashed) emission. A rough estimate of the expected experimental statistical error is given by the green dotted curve, where we anticipate an integrated luminosity of $300\,\text{fb}^{-1}$ and count all events in the relevant bin and in all bins with higher energies.

For the transverse momentum of the hardest jet (upper left plot in Fig. 8) the corrections are small ($\lesssim 2\%$) and negative close to the kinematical threshold. They become more and more negative with increasing momentum and amount to -20% for $p_{\text{T},j_1} = 1\,\text{TeV}$ and -30% for $p_{\text{T},j_1} = 2\,\text{TeV}$. The impact of real-subtracted photon emission is very small for the whole p_{T,j_1} range. In contrast the real-subtracted gluon emission is sensitive to the jet transverse momentum. With increasing p_{T,j_1} these interference contributions grow in size and reach $+8\%$ of the LO distribution at $p_{\text{T},j_1} = 2\,\text{TeV}$.[1] The comparison of the real-subtracted contributions with the full NLO result demonstrates that the virtual corrections dominate where high energy scales matter. This behaviour is governed by the Sudakov logarithms. For the whole p_{T,j_1} range up to 2 TeV we find the NLO corrections to be significant compared to the estimate of the statistical error. The relative corrections for the transverse momentum of the subleading jet (not shown) are similar to those of the leading jet in shape and size.

The relative EW corrections to the M_{jj} distribution (upper right plot in Fig. 8) stay between -2% and -9% for invariant masses up to 5 TeV. The corresponding real-subtracted photonic

[1] We find a noticeable real-subtracted gluon emission in distributions where the QCD corrections (see Ref. [28]) are large.

Process class	σ^{LO} [fb]	$\sigma^{\text{NLO}}_{\text{EW}}$ [fb]	$\frac{\sigma^{\text{NLO}}_{\text{EW}}}{\sigma^{\text{LO}}} - 1$ [%]
$ug \to ug\ell^-\ell^+$, $dg \to dg\ell^-\ell^+$, $\bar{u}g \to \bar{u}g\ell^-\ell^+$, $\bar{d}g \to \bar{d}g\ell^-\ell^+$	34584(8)	33729(8)	-2.41
$u\bar{u} \to gg\ell^-\ell^+$, $d\bar{d} \to gg\ell^-\ell^+$	2713(1)	2646(1)	-2.47
$gg \to u\bar{u}\ell^-\ell^+$, $gg \to d\bar{d}\ell^-\ell^+$	3612(1)	3532(1)	-2.21
$uu \to uu\ell^-\ell^+$, $dd \to dd\ell^-\ell^+$, $\bar{u}\bar{u} \to \bar{u}\bar{u}\ell^-\ell^+$, $\bar{d}\bar{d} \to \bar{d}\bar{d}\ell^-\ell^+$	1315.1(3)	1276.1(4)	-2.97
$u\bar{u} \to u'\bar{u}'\ell^-\ell^+$, $d\bar{d} \to d'\bar{d}'\ell^-\ell^+$, $u\bar{u}' \to u\bar{u}'\ell^-\ell^+$, $d\bar{d}' \to d\bar{d}'\ell^-\ell^+$	2463.7(5)	2388.1(7)	-3.07
$u\bar{u} \to d\bar{d}\ell^-\ell^+$, $d\bar{d} \to u\bar{u}\ell^-\ell^+$, $u\bar{u}' \to d\bar{d}'\ell^-\ell^+$, $d\bar{d}' \to u\bar{u}'\ell^-\ell^+$	438.82(7)	425.2(2)	-3.10
$ud \to u'd'\ell^-\ell^+$, $\bar{u}\bar{d} \to \bar{u}'\bar{d}'\ell^-\ell^+$, $ud \to ud\ell^-\ell^+$ $\bar{u}\bar{d} \to \bar{u}\bar{d}\ell^-\ell^+$ $uu' \to uu'\ell^-\ell^+$, $\bar{u}\bar{u}' \to \bar{u}\bar{u}'\ell^-\ell^+$ $dd' \to dd'\ell^-\ell^+$, $\bar{d}\bar{d}' \to \bar{d}\bar{d}'\ell^-\ell^+$	3856.8(7)	3766.5(8)	-2.34
$u\bar{d} \to u'\bar{d}'\ell^-\ell^+$, $\bar{u}d \to \bar{u}'d'\ell^-\ell^+$, $u\bar{d} \to u\bar{d}\ell^-\ell^+$, $\bar{u}d \to \bar{u}d\ell^-\ell^+$	2224.9(4)	2174.5(5)	-2.27
gluonic	40910(8)	39907(8)	-2.45
four-quark	10299(1)	10029(1)	-2.62
sum	51209(8)	49936(8)	-2.48

Table 3: NLO corrections to the total cross section for $pp \to jj\ell^-\ell^+$ at the 13 TeV LHC for basic cuts. In the first column the partonic processes are listed at LO. The second column provides the corresponding cross section including the NLO corrections. The third column contains the relative contribution to the total cross section in per cent.

corrections are also negative and below 2% in absolute value, and the real-subtracted gluonic corrections are even smaller. Note that for large M_{jj} the EW LO diagrams contribute 10−20% (see Fig. 3). Since we do not include EW corrections to these contributions, the full EW corrections are expected to be even larger than the results presented in Fig. 8. This explains the flattening of the relative EW corrections in the M_{jj} distribution to some extent.

The relative corrections for the transverse momentum of the negatively charged lepton and of the lepton pair are presented in the second row of Fig. 8. The NLO corrections are again negative but larger in absolute size for p_{T,ℓ^-} than for the corresponding p_{T,j_1}. For $p_{T,\ell^-} = 200\,\text{GeV}$ we find corrections of −10% and for p_{T,ℓ^-} values around 1 TeV the corrections are of the order of −30%. The contribution from real-subtracted photon emission behaves similarly as in the p_{T,j_1} case and remains small over the whole p_{T,ℓ^-} range. We observe that the contribution of real-subtracted gluon emission remains at the per-mille level. For $p_{T,\ell^-} \simeq 1400\,\text{GeV}$ the estimate of the statistical error becomes of the same size as the NLO corrections. The relative corrections to the distribution in the transverse momentum of the positively charged lepton (not shown) are similar in shape but smaller in magnitude (−22% at $p_{T,\ell^+} \simeq 1\,\text{TeV}$). The relative corrections

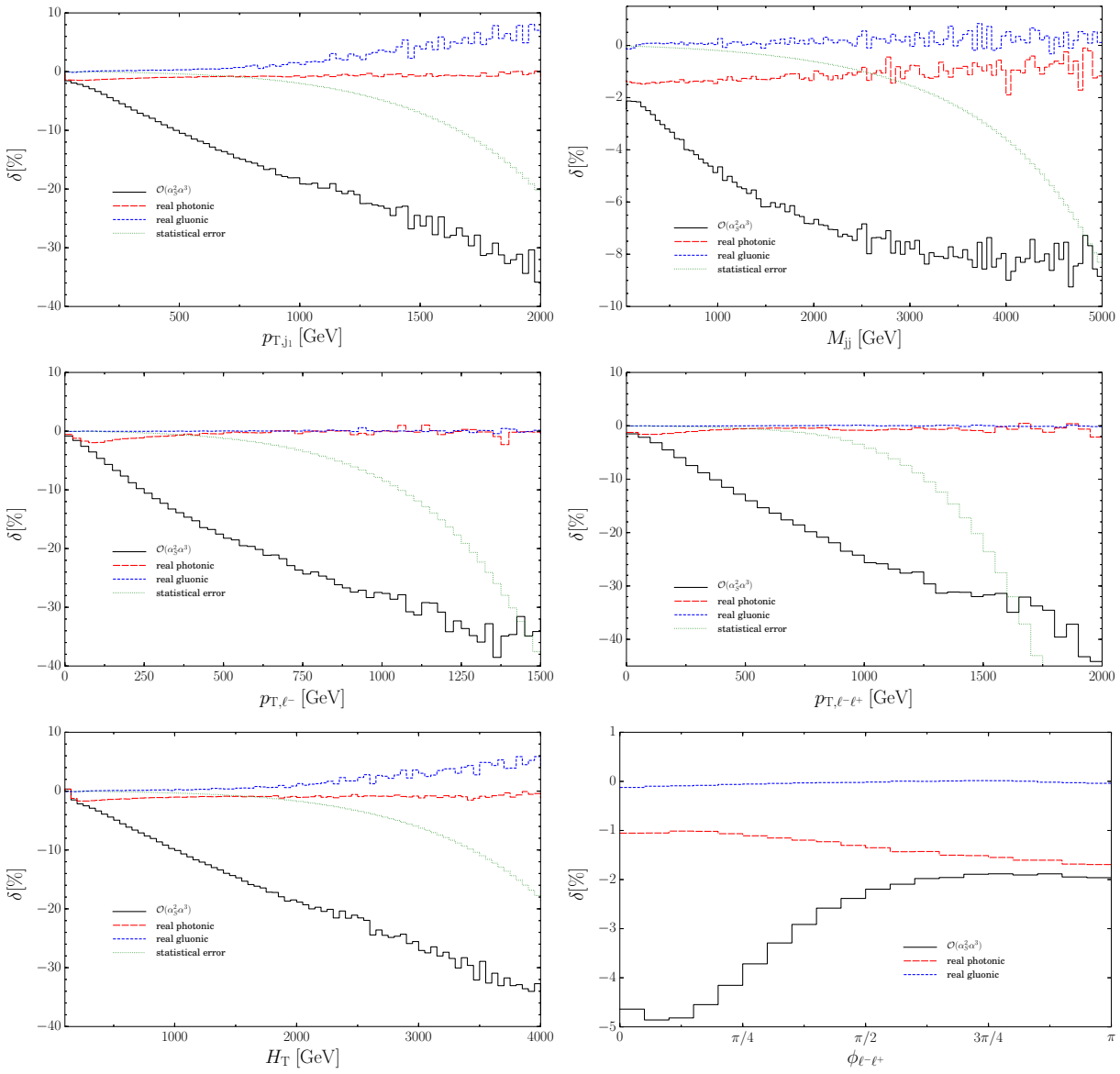

Figure 8: Relative $\mathcal{O}(\alpha_s^2\alpha^3)$ corrections in per cent at the 13 TeV LHC for basic cuts to the distributions in the transverse momentum of the harder jet j_1, the di-jet invariant mass M_{jj}, the transverse momenta of the negatively charged lepton ℓ^- and the lepton pair $\ell^-\ell^+$, the scalar sum of all transverse momenta, and the relative azimuthal angle between the leptons. Further details are described in the text.

to the distribution in the transverse momentum of the lepton pair are again dominated by the virtual corrections and reach -24% at $p_{\mathrm{T},\ell^-\ell^+} \simeq 1\,\mathrm{TeV}$.

The relative corrections to the scalar sum of all transverse momenta H_T as defined in (2.20), shown in the lower left plot of Fig. 8, exhibit a similar behaviour as for the previously discussed p_T distributions. For $H_\mathrm{T} = 2(4)\,\mathrm{TeV}$ we find the NLO corrections to be of the order of -20% (-35%). As for $p_{\mathrm{T},\mathrm{j}_1}$ the relative corrections induced by real-subtracted gluon emission are positive and rise with increasing energy, while the real-subtracted photon emission remains at the -1% level. The estimate of the statistical error demonstrates that for $300\,\mathrm{fb}^{-1}$ the corrections are relevant up to $H_\mathrm{T} = 4{-}5\,\mathrm{TeV}$.

The relative NLO corrections to the azimuthal angle between the leptons are shown in the lower right plot of Fig. 8. Since the angle between the leptons is an energy-independent observable we do not observe any Sudakov enhancement. Nevertheless it is interesting that the NLO corrections induce non-uniform shape changes. For angles $\phi_{\ell^-\ell^+} \lesssim \pi/2$ the relative corrections are of the order of -5%. Above $\phi_{\ell^-\ell^+} \simeq \pi/2$ they decrease in absolute value with increasing angle. For $\phi_{\ell^-\ell^+} \simeq \pi$ the NLO corrections reach -2% and stay constant for higher $\phi_{\ell^-\ell^+}$ values. It is interesting to note that the shape of the relative corrections is essentially determined by the virtual corrections. While the corrections from real-subtracted photon emission dominate for $\phi_{\ell^-\ell^+} \gtrsim \pi/2$, the contribution from real-subtracted gluon emission is always below 2‰.

The relative corrections to the distributions in the rapidities of the jets and leptons are essentially flat (with a variation $\lesssim 1\%$).

3.5 Results for vector-boson-fusion cuts

In this section we present NLO results for the total cross section and various differential distributions using the input parameters (2.7) and acceptance cuts (2.15), (2.16), (2.17), and (2.21). In Table 4 we show the impact of the NLO corrections on the various subprocesses. The corrections to the partonic total cross sections are again negative for all process classes. The spread of the corrections for the different channels is somewhat larger as for basic cuts ranging from -3.4% to -2.2% and the correction for the total hadronic cross section amounts to -2.7%. The relative correction for the channels of type $u\bar{u} \to d\bar{d}\ell^-\ell^+$ should be regarded with care. These channels are dominated by LO EW diagrams (see Table 2), for which the EW corrections are not included in our calculation. The full EW corrections might be different for these channels. This caveat applies to a lesser extent also to the channels of type $ud \to u'd'\ell^-\ell^+$, while for all other channels and for the sums the EW corrections to the LO EW diagrams are negligible.

In Fig. 9 we present the effects of the NLO electroweak corrections on differential distributions for VBF cuts using the same style as in Fig. 8. For all considered distributions we find relative corrections from subtracted real photon and real gluon contributions below $\sim 2\%$ and $\sim 1\%$, respectively. Thus, in particular for high energy scales, the virtual corrections and more precisely the Sudakov corrections dominate again. The effects of the total $\mathcal{O}(\alpha_\mathrm{s}^3\alpha^2)$ corrections are qualitatively similar as for basic cuts, but quantitatively we find some differences.

For the transverse momentum of the hardest jet (upper left plot in Fig. 9) the EW corrections are somewhat larger as for basic cuts and reach -25% for $p_{\mathrm{T},\mathrm{j}_1} = 1\,\mathrm{TeV}$. For the transverse momentum of the second hardest jet (not shown), the corrections are similar as for basic cuts. For the di-jet invariant mass distribution the corrections are somewhat smaller and do not exceed -6% (upper right plot in Fig. 9). Note, however, that in this case the EW LO diagrams amount up to 50% and the missing EW corrections to these contributions could enhance the EW corrections even by a factor 2.

Process class	σ^{LO} [fb]	$\sigma^{\text{NLO}}_{\text{EW}}$ [fb]	$\frac{\sigma^{\text{NLO}}_{\text{EW}}}{\sigma^{\text{LO}}} - 1$ [%]
$ug \to ug\ell^-\ell^+$, $dg \to dg\ell^-\ell^+$, $\bar{u}g \to \bar{u}g\ell^-\ell^+$, $\bar{d}g \to \bar{d}g\ell^-\ell^+$	540.9(3)	524.0(3)	-3.12
$u\bar{u} \to gg\ell^-\ell^+$, $d\bar{d} \to gg\ell^-\ell^+$	22.35(1)	21.80(1)	-2.46
$gg \to u\bar{u}\ell^-\ell^+$, $gg \to d\bar{d}\ell^-\ell^+$	54.53(2)	53.34(3)	-2.18
$uu \to uu\ell^-\ell^+$, $dd \to dd\ell^-\ell^+$, $\bar{u}\bar{u} \to \bar{u}\bar{u}\ell^-\ell^+$, $\bar{d}\bar{d} \to \bar{d}\bar{d}\ell^-\ell^+$	86.22(5)	83.31(7)	-3.38
$u\bar{u} \to u'\bar{u}'\ell^-\ell^+$, $d\bar{d} \to d'\bar{d}'\ell^-\ell^+$, $u\bar{u}' \to u\bar{u}'\ell^-\ell^+$, $d\bar{d}' \to d\bar{d}'\ell^-\ell^+$	65.98(3)	63.76(4)	-3.36
$u\bar{u} \to d\bar{d}\ell^-\ell^+$, $d\bar{d} \to u\bar{u}\ell^-\ell^+$, $u\bar{u}' \to d\bar{d}'\ell^-\ell^+$, $d\bar{d}' \to u\bar{u}'\ell^-\ell^+$	21.198(7)	20.905(7)	-1.38
$ud \to u'd'\ell^-\ell^+$, $\bar{u}\bar{d} \to \bar{u}'\bar{d}'\ell^-\ell^+$, $ud \to ud\ell^-\ell^+$, $\bar{u}\bar{d} \to \bar{u}\bar{d}\ell^-\ell^+$ $uu' \to uu'\ell^-\ell^+$, $\bar{u}\bar{u}' \to \bar{u}\bar{u}'\ell^-\ell^+$ $dd' \to dd'\ell^-\ell^+$, $\bar{d}\bar{d}' \to \bar{d}\bar{d}'\ell^-\ell^+$	180.61(8)	176.3(1)	-2.39
$u\bar{d} \to u'\bar{d}'\ell^-\ell^+$, $\bar{u}d \to \bar{u}'d'\ell^-\ell^+$, $u\bar{d} \to u\bar{d}\ell^-\ell^+$, $\bar{u}d \to \bar{u}d\ell^-\ell^+$	67.73(2)	65.92(3)	-2.67
gluonic	617.8(4)	599.2(3)	-3.01
four-quark	421.7(1)	410.2(1)	-2.73
sum	1039.6(4)	1009.3(3)	-2.91

Table 4: NLO corrections to the total cross section for $pp \to jj\ell^-\ell^+$ at the 13 TeV LHC for VBF cuts. In the first column the partonic processes are listed at LO. The second column provides the corresponding cross section including the NLO corrections. The third column contains the relative contribution to the total cross section in per cent.

The relative corrections for the transverse momentum of the negatively charged lepton are shown in the middle left plot of Fig. 9. The NLO corrections are somewhat smaller in absolute size than for the same distribution with basic cuts and do not exceed -20% even for $p_{\text{T},\ell^-} = 750\,\text{GeV}$. For $p_{\text{T},\ell^-} \simeq 700\,\text{GeV}$ the estimate of the statistical error becomes of the same size as the NLO corrections. The relative corrections to the distribution in the transverse momentum of the positively charged lepton (not shown) are again smaller in magnitude (-17% at 750 GeV). The distribution in the transverse momentum of the lepton pair (middle left plot in Fig. 9) receives EW corrections of -25% at $p_{\text{T},\ell^-\ell^+} \simeq 1\,\text{TeV}$.

The relative corrections to the scalar sum of all transverse momenta H_{T} shown in the lower left plot of Fig. 9 behave similar as those for the $p_{\text{T,j}_1}$ distribution. They are larger as for basic cuts and are relevant up to $H_{\text{T}} = 2\,\text{TeV}$ for $300\,\text{fb}^{-1}$.

The relative NLO corrections to the azimuthal angle between the leptons are depicted in the lower right plot of Fig. 9. For VBF cuts the real photonic corrections vary between 1% and -1%. The complete EW corrections range between -2% and -4%.

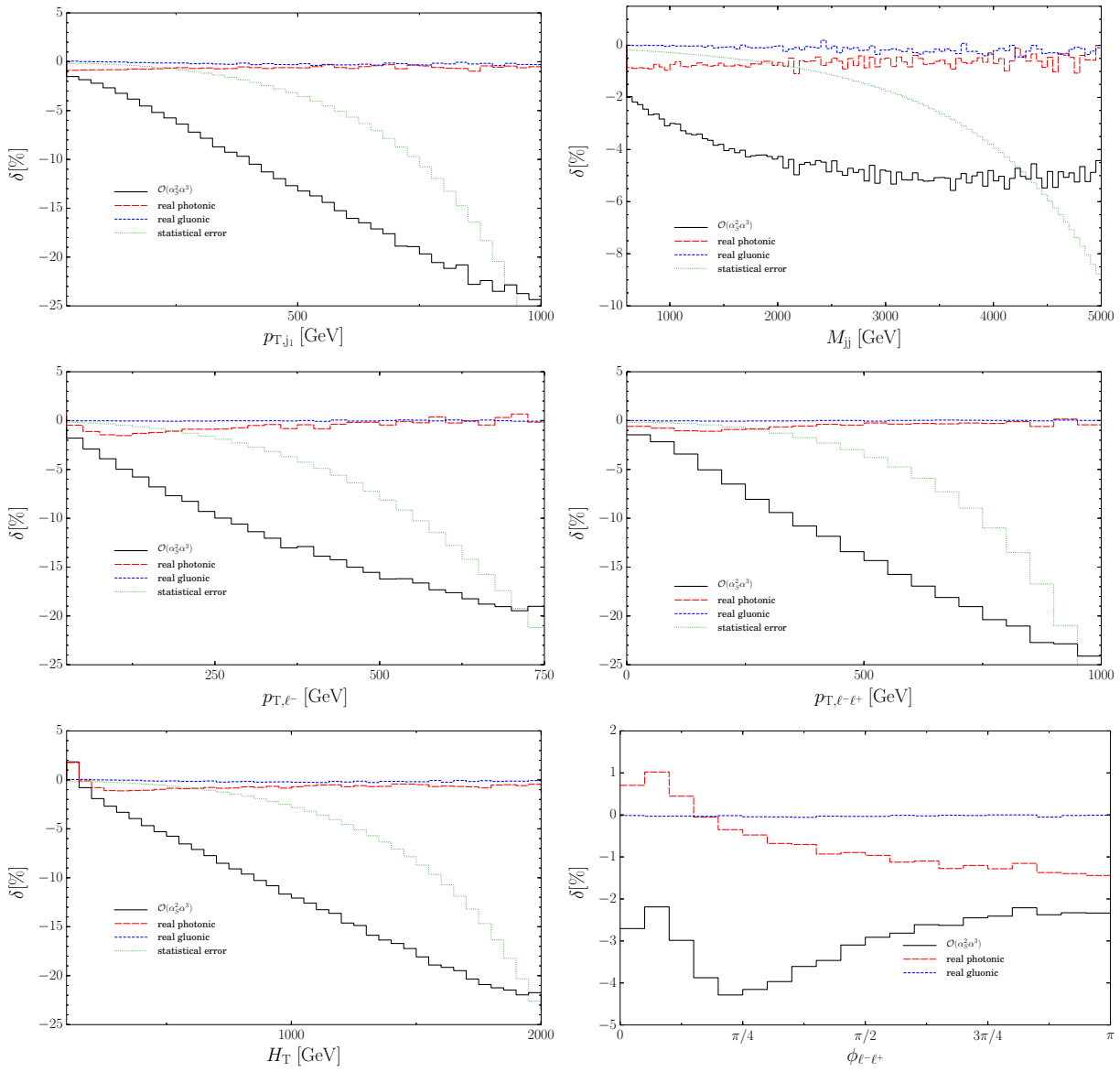

Figure 9: Relative $\mathcal{O}(\alpha_s^2\alpha^3)$ corrections in per cent at the 13 TeV LHC for VBF cuts to the distributions in the transverse momentum of the harder jet j_1, the di-jet invariant mass M_{jj}, the transverse momenta of the negatively charged lepton ℓ^- and the lepton pair $\ell^-\ell^+$, the scalar sum of all transverse momenta, and the relative azimuthal angle between the leptons. Further details are described in the text.

While the relative real corrections to the distributions in the rapidities of the jets and leptons are still relatively flat, the virtual corrections induce variations at the level of two per cent.

4 Conclusions

We have calculated the electroweak corrections to the production of lepton pairs in association with two jets at the LHC. More precisely, we have computed the corrections of absolute order $\mathcal{O}(\alpha_s^2\alpha^3)$, consisting of electroweak corrections to the squared leading-order QCD diagrams and QCD corrections to the leading-order QCD–EW interferences, for the full process $pp \to jj\ell^-\ell^+$ including all off-shell effects. The calculation has been performed with the recursive matrix element generator Recola and the one-loop integral library Collier and demonstrates the strength of these codes for multiparticle NLO calculations. For the phase-space integration we use multi-channel Monte-Carlo techniques, dipole subtraction and the fragmentation function to separate photons and jets.

We have discussed results for total cross sections and various distributions within a basic set of cuts and within a set of cuts typical for vector-boson fusion. Electroweak corrections change the total cross sections by a few per cent and distort angular distributions at a similar level. However, in the high-energy tails of invariant-mass and transverse-momentum distributions the electroweak corrections amount to several tens of per cent and are typically larger than the expected experimental errors. These large effects can be traced back to the virtual corrections and thus to the Sudakov logarithms.

Acknowledgements

This work was supported in part by the Deutsche Forschungsgemeinschaft (DFG) under reference number DE 623/2-1. The work of L.H. was supported by the grant FPA2011-25948.

A Appendix

In the following we describe our implementation of the photon fragmentation in the context of the dipole method for a consistent recombination of photons and jets. We follow closely Refs. [34, 57] but instead of regularising IR singularities by infinitesimal photon and fermion masses we apply dimensional regularisation. Furthermore, we have generalised the results to include the α-dependent subtraction terms introduced in Refs. [54–56] which allow to vary the size of the subtraction region in phase space.

In the framework of the subtraction procedure [53] the NLO cross-section for the process $pp \to jj\ell^-\ell^+$ can schematically be written as

$$\mathrm{d}\sigma_{\mathrm{NLO}} = \int_{n+1} \Big[\mathrm{d}\sigma_{\mathrm{real}} - \mathrm{d}\sigma_{\mathrm{dipole}}\Big] \;+\; \int_{n} \Big[\mathrm{d}\sigma_{\mathrm{virtual}} + \int_{1} \mathrm{d}\sigma_{\mathrm{dipole}}\Big], \tag{A.1}$$

where adding and subtracting the dipole contribution $\mathrm{d}\sigma_{\mathrm{dipole}}$ renders the n- and the $(n+1)$-dimensional phase-space integrals separately IR-finite (in our case $n = 4$). When calculating photonic NLO corrections for processes with final-state quarks and gluons, however, the above procedure suffers from IR-unsafe configurations in $\mathrm{d}\sigma_{\mathrm{real}}$ arising from the recombination of a gluon with a hard photon to form a jet. Such jets that are dominated by hard photons are called *hard-photon jets* in the following.

Since a recombined $g\gamma$ configuration with a soft gluon forms part of the NLO QCD corrections to the process $pp \to \ell^-\ell^+j\gamma$, the corresponding IR singularity is not cancelled by the QED dipole

term $\mathrm{d}\sigma_{\mathrm{dipole}}$ constructed for the NLO QED corrections to the process $\mathrm{pp} \to \mathrm{jj}\ell^-\ell^+$. To solve this problem we slightly modify the jet algorithm such that hard-photon jets are discarded. For the recombination of a QCD parton with energy E_a and a photon with energy E_γ we consider the photon-jet energy fraction

$$z_\gamma = \frac{E_\gamma}{E_\gamma + E_a}. \tag{A.2}$$

The type of the recombined particle is then determined as a function of z_γ. For $z_\gamma < z_{\gamma,\mathrm{cut}}$ we treat the recombined particle as a jet, for $z_\gamma > z_{\gamma,\mathrm{cut}}$ as a photon. Using this criterion to reject hard-photon jets, (A.1) becomes

$$\begin{aligned}\mathrm{d}\sigma_{\mathrm{NLO}} = {} & \int_{n+1} \theta(z_{\gamma,\mathrm{cut}} - z_\gamma)\Big[\mathrm{d}\sigma_{\mathrm{real}} - \mathrm{d}\sigma_{\mathrm{dipole}}\Big] \quad + \\ & \int_n \Big[\mathrm{d}\sigma_{\mathrm{virtual}} + \int_1 \Big(\mathrm{d}\sigma_{\mathrm{dipole}} - \mathrm{d}\sigma^{\gamma\ \mathrm{coll}}_{\mathrm{dipole}}(z_{\gamma,\mathrm{cut}})\Big) - \mathrm{d}\sigma_{\mathrm{frag}}(z_{\gamma,\mathrm{cut}})\Big].\end{aligned} \tag{A.3}$$

Inside the n-dimensional phase-space integral the rejection of jets dominated by hard photons leads to a modification of the original dipole contribution by the additional term

$$\mathrm{d}\sigma^{\gamma\ \mathrm{coll}}_{\mathrm{dipole}}(z_{\gamma,\mathrm{cut}}) = \theta(z_\gamma - z_{\gamma,\mathrm{cut}})\mathrm{d}\sigma_{\mathrm{dipole}}. \tag{A.4}$$

Further, since the final state is not fully inclusive anymore, contributions in which the final-state quark fragments into a hard photon have to be subtracted by means of

$$\mathrm{d}\sigma_{\mathrm{frag}}(z_{\gamma,\mathrm{cut}}) = \sum_i \mathrm{d}\sigma_{\mathrm{born}} \int_{z_{\gamma,\mathrm{cut}}}^1 \mathrm{d}z_\gamma\ D_{q_i\to\gamma}(z_\gamma)\,, \tag{A.5}$$

where $D_{q_i\to\gamma}$ is the quark-to-photon fragmentation function and the sum covers all quarks q_i in the final state.

Since photon fragmentation is related to final-state singularities, only dipoles with final-state emitter are affected and are considered in the following. The results for gluon emission from final-state quarks of Refs. [53, 55] can easily be transferred to the photon case by replacing $\alpha_s \to \alpha$ and $C_F \to Q^2$, and by substituting colour-correlated matrix elements by their charge-weighted counterparts

$$Q_i\sigma_i Q_j\sigma_j|\mathcal{M}_{\mathrm{born}}|^2. \tag{A.6}$$

Here, $Q_{i,j}$ represent the charges of the emitter and spectator quarks ($Q_{i,j} = 2/3$ for up-type and $Q_{i,j} = -1/3$ for down-type quarks), while $\sigma_{i,j}$ denotes the corresponding charge flow ($\sigma_{i,j} = +1$ for incoming quarks and outgoing anti-quarks, $\sigma_{i,j} = -1$ for incoming anti-quarks and outgoing quarks). The integrated dipole contribution $\int_1 \mathrm{d}\sigma_{\mathrm{dipole}}$ for *final-state emitter with final-state spectator* can be obtained from eq. (5.32) of Ref. [53] and adding the α-dependent terms of eq. (11) of Ref. [55] reads

$$\mathcal{V}_{qg}(\alpha,\epsilon) = Q_q^2\left(\frac{1}{\epsilon^2} + \frac{3}{2\epsilon} + 5 - \frac{\pi^2}{2} - \ln^2\alpha + \frac{3}{2}(\alpha - 1 - \ln\alpha)\right). \tag{A.7}$$

For *final-state emitter with initial-state spectator* the α-extended version of eq. (5.57) of Ref. [53] can be obtained from eqs. (5.50) and (5.54) of this paper by restricting the integration range of x to the interval $[1-\alpha, 1]$ resulting in

$$\begin{aligned}\mathcal{V}_{qg}(x;\alpha,\epsilon) = {} & Q_q^2\Bigg\{\left(\frac{2}{1-x}\ln\frac{1}{1-x}\right)_{1-\alpha} - \frac{3}{2}\left(\frac{1}{1-x}\right)_{1-\alpha} + \Theta(x-1+\alpha)\frac{2}{1-x}\ln(2-x) \\ & + \delta(1-x)\left[\mathcal{V}_{qg}(1,\epsilon) - \frac{3}{2} - \ln^2\alpha - \frac{3}{2}\ln\alpha\right]\Bigg\}.\end{aligned} \tag{A.8}$$

The $(1-\alpha)$ - distribution is a modification of the usual +-distribution and defined as

$$\int_0^1 \mathrm{d}x\ f(x)_{1-\alpha} g(x) = \int_{1-\alpha}^1 \mathrm{d}x\ f(x)\left[g(x) - g(1)\right]. \tag{A.9}$$

The additional dipole subtraction term $\int_1 \mathrm{d}\sigma^{\gamma\,\mathrm{coll}}_{\mathrm{dipole}}$ can be represented in a completely analogous manner. For *final-state emitter with final-state spectator* it results from eqs. (5.28) and (5.29) of Ref. [53] by restricting the y integration by α and the z integration by $z_{\gamma,\mathrm{cut}}$,

$$\begin{aligned}
\mathcal{V}^{\gamma\,\mathrm{coll}}_{qg}(x;\alpha,\epsilon,z_{\gamma,\mathrm{cut}}) &= Q_q^2 \int_0^{1-z_{\gamma,\mathrm{cut}}} \mathrm{d}z\,(z(1-z))^{-\epsilon} \int_0^{\alpha} \mathrm{d}y\, y^{-\epsilon-1}(1-y)^{1-2\epsilon} \\
&\qquad \times \left[\frac{2}{1-z+yz} - (1+z) - \epsilon(1-z)\right] \\
&= Q_q^2 \int_0^{1-z_{\gamma,\mathrm{cut}}} \mathrm{d}z \left\{ \frac{1+z^2}{1-z}\left(-\frac{1}{\epsilon} + \ln[z(1-z)] + \ln\alpha\right) + \alpha(1+z) + 1 - z \right. \\
&\qquad \left. - \frac{2}{z(1-z)} \ln\left(\frac{1-z+\alpha z}{1-z}\right)\right\}.
\end{aligned} \tag{A.10}$$

Similarly the contribution from *final-state emitter with initial-state spectator* to the additional dipole subtraction term is obtained from eqs. (5.50) and (5.54) of Ref. [53] upon using appropriate integration boundaries

$$\begin{aligned}
\mathcal{V}^{\gamma\,\mathrm{coll}}_{qg}(x;\alpha,\epsilon,z_{\gamma,\mathrm{cut}}) &= Q_q^2 \theta(1-x)\theta(x-1+\alpha)(1-x)^{-1-\epsilon} \int_0^{1-z_{\gamma,\mathrm{cut}}} \mathrm{d}z\,(z(1-z))^{-\epsilon} \\
&\qquad \times \left[\frac{2}{2-z-x} - (1+z) - \epsilon(1-z)\right] \\
&= Q_q^2 \int_0^{1-z_{\gamma,\mathrm{cut}}} \mathrm{d}z \left\{ \left[\frac{1}{1-x}\left(\frac{2}{2-z-x} - 1 - z\right)\right]_{1-\alpha} \right. \\
&\qquad + \delta(1-x)\left[\frac{1+z^2}{1-z}\left(-\frac{1}{\epsilon} + \ln[z(1-z)] + \ln\alpha\right)\right. \\
&\qquad \left.\left. + (1-z) - \frac{2}{1-z}\ln\left(\frac{1-z+\alpha}{1-z}\right)\right]\right\}.
\end{aligned} \tag{A.11}$$

Equations (A.10) and (A.11) contain collinear singularities which are cancelled by the contribution $\mathrm{d}\sigma_{\mathrm{frag}}$ once the photon fragmentation function $D_{q_i\to\gamma}$ is renormalised, reflecting the IR-safety of our event definition. To this end we follow closely the procedure in Refs. [34, 57] and relate $D_{q_i\to\gamma}$ to the parametrisation $D^{\mathrm{ALEPH},\ \overline{\mathrm{MS}}}_{q\to\gamma}$ measured at ALEPH [59]. We find

$$D_{q\to\gamma} = \frac{\alpha Q_q^2}{2\pi} P_{q\to\gamma}(z_\gamma)\left[\frac{(4\pi)^\epsilon}{\Gamma(1-\epsilon)}\frac{1}{\epsilon} + \ln\left(\frac{\mu^2}{\mu_{\mathrm{F}}^2}\right)\right] + D^{\mathrm{ALEPH},\ \bar{\mathrm{MS}}}_{q\to\gamma}(z_\gamma,\mu_{\mathrm{F}}), \tag{A.12}$$

where we identify

$$P_{q\to\gamma}(z_\gamma) = \frac{1+(1-z_\gamma)^2}{z_\gamma} \xrightarrow{z_\gamma = 1-z} \frac{1+z^2}{1-z} \tag{A.13}$$

and

$$D^{\mathrm{ALEPH},\ \overline{\mathrm{MS}}}_{q\to\gamma}(1-z,\mu_{\mathrm{F}}) = \frac{\alpha Q_q^2}{2\pi}\left[\frac{1+z^2}{1-z}\ln\left(\frac{\mu_{\mathrm{F}}^2}{z^2\mu_0^2}\right) + C\right]. \tag{A.14}$$

The μ_F-dependence of the photon fragmentation function cancels by construction. The constants μ_0 and C are fit parameters extracted from the experimental measurement [59]. They are given as

$$\mu_0 = 0.14\,\text{GeV}, \quad C = -13.26. \tag{A.15}$$

References

[1] M. Ciccolini, A. Denner and S. Dittmaier, Phys. Rev. D **77** (2008) 013002 [arXiv:0710.4749 [hep-ph]].

[2] J. Butterworth, *et al.*, Les Houches 2013: Physics at TeV Colliders: Standard Model Working Group Report, arXiv:1405.1067 [hep-ph].

[3] T. Hahn and M. Perez-Victoria, Comput. Phys. Commun. **118** (1999) 153 [hep-ph/9807565].

[4] K. Arnold *et al.*, Comput. Phys. Commun. **180** (2009) 1661 [arXiv:0811.4559 [hep-ph]].

[5] C. F. Berger *et al.*, Phys. Rev. D **78** (2008) 036003 [arXiv:0803.4180 [hep-ph]].

[6] S. Becker, C. Reuschle and S. Weinzierl, JHEP **1012** (2010) 013 [arXiv:1010.4187 [hep-ph]].

[7] S. Badger, B. Biedermann and P. Uwer, Comput. Phys. Commun. **182** (2011) 1674 [arXiv:1011.2900 [hep-ph]].

[8] V. Hirschi *et al.*, JHEP **1105** (2011) 044 [arXiv:1103.0621 [hep-ph]].

[9] G. Bevilacqua *et al.*, Comput. Phys. Commun. **184** (2013) 986 [arXiv:1110.1499 [hep-ph]].

[10] G. Cullen *et al.*, Eur. Phys. J. C **72** (2012) 1889 [arXiv:1111.2034 [hep-ph]].

[11] F. Cascioli, P. Maierhöfer and S. Pozzorini, Phys. Rev. Lett. **108** (2012) 111601 [arXiv:1111.5206 [hep-ph]].

[12] S. Frixione, V. Hirschi, D. Pagani, H. S. Shao and M. Zaro, JHEP **1409** (2014) 065 [arXiv:1407.0823 [hep-ph]].

[13] G. Cullen, *et al.*, arXiv:1404.7096 [hep-ph].

[14] S. Actis, A. Denner, L. Hofer, A. Scharf and S. Uccirati, JHEP **1304** (2013) 037 [arXiv:1211.6316 [hep-ph]].

[15] S. Actis, A. Denner, L. Hofer, A. Scharf and S. Uccirati, PoS LL **2014** (2014) 023.

[16] A. van Hameren, JHEP **0907** (2009) 088 [arXiv:0905.1005 [hep-ph]].

[17] A. Denner, S. Dittmaier and L. Hofer, in preparation.

[18] A. Denner, S. Dittmaier and L. Hofer, PoS LL **2014** (2014) 071 [arXiv:1407.0087 [hep-ph]].

[19] V. A. Khoze, M. G. Ryskin, W. J. Stirling and P. H. Williams, Eur. Phys. J. C **26** (2003) 429 [hep-ph/0207365].

[20] C. Oleari and D. Zeppenfeld, Phys. Rev. D **69** (2004) 093004 [hep-ph/0310156].

[21] G. Aad *et al.* [ATLAS Collaboration], JHEP **1307** (2013) 032 [arXiv:1304.7098 [hep-ex]].

[22] CMS Collaboration [CMS Collaboration], CMS-PAS-SMP-12-017.

[23] CMS Collaboration [CMS Collaboration], CMS-PAS-SMP-14-009.

[24] S. Chatrchyan *et al.* [CMS Collaboration], JHEP **1310** (2013) 101 [arXiv:1305.7389 [hep-ex]].

[25] V. Khachatryan *et al.* [CMS Collaboration], arXiv:1410.3153 [hep-ex].

[26] G. Aad *et al.* [ATLAS Collaboration], JHEP **1404** (2014) 031 [arXiv:1401.7610 [hep-ex]].

[27] J. M. Campbell and R. K. Ellis, Phys. Rev. D **65** (2002) 113007 [hep-ph/0202176].

[28] J. M. Campbell, R. K. Ellis and D. L. Rainwater, Phys. Rev. D **68** (2003) 094021 [hep-ph/0308195].

[29] E. Re, JHEP **1210** (2012) 031 [arXiv:1204.5433 [hep-ph]].

[30] J. M. Campbell, R. K. Ellis, P. Nason and G. Zanderighi, JHEP **1308** (2013) 005 [arXiv:1303.5447 [hep-ph]].

[31] B. Jäger, S. Schneider and G. Zanderighi, JHEP **1209** (2012) 083 [arXiv:1207.2626 [hep-ph]].

[32] F. Schissler and D. Zeppenfeld, JHEP **1304** (2013) 057 [arXiv:1302.2884].

[33] M. Chiesa, *et al.*, Phys. Rev. Lett. **111** (2013) 12, 121801 [arXiv:1305.6837 [hep-ph]].

[34] A. Denner, S. Dittmaier, T. Kasprzik and A. Mück, JHEP **0908** (2009) 075 [arXiv:0906.1656 [hep-ph]].

[35] A. Denner, S. Dittmaier, T. Kasprzik and A. Mück, JHEP **1106** (2011) 069 [arXiv:1103.0914 [hep-ph]].

[36] A. Denner, S. Dittmaier, T. Kasprzik and A. Mück, Eur. Phys. J. C **73** (2013) 2297 [arXiv:1211.5078 [hep-ph]].

[37] A. Denner, S. Dittmaier, M. Roth and D. Wackeroth, Nucl. Phys. B **560** (1999) 33 [hep-ph/9904472].

[38] A. Denner, S. Dittmaier, M. Roth and L. H. Wieders, Nucl. Phys. B **724** (2005) 247 [Erratum-ibid. B **854** (2012) 504] [hep-ph/0505042].

[39] A. Denner and S. Dittmaier, Nucl. Phys. Proc. Suppl. **160** (2006) 22 [hep-ph/0605312].

[40] D. Y. Bardin, A. Leike, T. Riemann and M. Sachwitz, Phys. Lett. B **206** (1988) 539.

[41] J. Beringer *et al.* [Particle Data Group Collaboration], Phys. Rev. D **86** (2012) 010001.

[42] Tevatron Electroweak Working Group and CDF and D0 Collaborations, arXiv:1107.5255 [hep-ex].

[43] A. D. Martin *et al.*, Eur. Phys. J. C **63**, (2009) 189 [arXiv:0901.0002 [hep-ph]].

[44] M. Cacciari, G. P. Salam and G. Soyez, JHEP **0804** (2008) 063 [arXiv:0802.1189 [hep-ph]].

[45] R. D. Ball *et al.* [NNPDF Collaboration], Nucl. Phys. B **877** (2013) 290 [arXiv:1308.0598 [hep-ph]].

[46] S. Moretti, M. R. Nolten and D. A. Ross, Nucl. Phys. B **759** (2006) 50 [hep-ph/0606201].

[47] A. Scharf, in Proceedings of the "Meeting of the Division of the American Physical Society, DPF 2009", arXiv:0910.0223 [hep-ph].

[48] A. Denner and S. Dittmaier, Nucl. Phys. B **658** (2003) 175 [hep-ph/0212259].

[49] A. Denner and S. Dittmaier, Nucl. Phys. B **734** (2006) 62 [hep-ph/0509141].

[50] W. Beenakker and A. Denner, Nucl. Phys. B **338** (1990) 349.

[51] A. Denner, U. Nierste and R. Scharf, Nucl. Phys. B **367** (1991) 637.

[52] A. Denner and S. Dittmaier, Nucl. Phys. B **844** (2011) 199 [arXiv:1005.2076 [hep-ph]].

[53] S. Catani and M. H. Seymour, Nucl. Phys. B **485** (1997) 291 [Erratum-ibid. B **510** (1998) 503] [hep-ph/9605323].

[54] Z. Nagy and Z. Trocsanyi, Phys. Rev. D **59** (1999) 014020 [Erratum-ibid. D **62** (2000) 099902] [hep-ph/9806317].

[55] Z. Nagy, Phys. Rev. D **68** (2003) 094002 [hep-ph/0307268].

[56] J. M. Campbell, R. K. Ellis and F. Tramontano, Phys. Rev. D **70** (2004) 094012 [hep-ph/0408158].

[57] A. Denner, S. Dittmaier, T. Gehrmann and C. Kurz, Nucl. Phys. **B836** (2010) 37 [arXiv:1003.0986 [hep-ph]].

[58] E. W. N. Glover and A. G. Morgan, Z. Phys. C **62** (1994) 311.

[59] D. Buskulic *et al.* [ALEPH Collaboration], Z. Phys. C **69** (1996) 365.

[60] T. Motz, PhD thesis, Zürich 2011.

[61] T. Hahn, Comput. Phys. Commun. **140** (2001) 418 [hep-ph/0012260].

[62] T. Hahn and C. Schappacher, Comput. Phys. Commun. **143** (2002) 54 [hep-ph/0105349].

[63] E. Accomando, A. Denner and C. Meier, Eur. Phys. J. C **47** (2006) 125 [hep-ph/0509234].

[64] S. Dittmaier and M. Roth, Nucl. Phys. B **642** (2002) 307 [hep-ph/0206070].

[65] A. Denner, L. Hofer, A. Scharf and S. Uccirati, PoS RADCOR **2013** (2013) 019 [arXiv:1311.5336 [hep-ph]].